Acta Materialia 166 (2019) 386–401

Contents lists available at ScienceDirect

Acta Materialia

journal homepage: www.elsevier.com/locate/actamat

Full length article

A crystallographic extension to the Olson-Cohen model for predicting strain path dependence of martensitic transformation

Milovan Zecevic [a], Manas V. Upadhyay [b], Efthymios Polatidis [c], Tobias Panzner [c], Helena Van Swygenhoven [b, d], Marko Knezevic [a, *]

[a] Department of Mechanical Engineering, University of New Hampshire, Durham, NH, 03824, USA
[b] Swiss Light Source, Paul Scherrer Institute, CH-5232 Villigen PSI, Switzerland
[c] Laboratory for Neutron Scattering, NUM, Paul Scherrer Institute, Villigen PSI, 5232, Switzerland
[d] Neutrons and X-rays for Mechanics of Materials, IMX, Ecole Polytechnique Federale de Lausanne, CH-1012, Lausanne, Switzerland

ARTICLE INFO

Article history:
Received 8 October 2018
Received in revised form
18 December 2018
Accepted 31 December 2018
Available online 3 January 2019

Keywords:
Phase transformation
Microstructures
Polycrystalline material
Crystal plasticity
Austenitic steel

ABSTRACT

A modification to the empirical Olson-Cohen strain-induced austenite to martensite transformation kinetic model is proposed. The proposed kinetic model accounts for the stress state at the grain level and the crystallography of the transformation mechanism. Two transformation mechanisms sensitive to the local stress state are incorporated in the model. First, the resolved shear stress on a slip plane in the direction perpendicular to the Burgers vector determines the stacking fault width (SFW) which in turn determines the potential nucleation sites. Second, the stress triaxiality governs the probability of the structural α'-martensite formation at a nucleation site. The kinetic model is implemented in the elasto-plastic self-consistent (EPSC) crystal plasticity model to study the stress state and texture dependence of the strain-induced α'-martensite transformation and the mechanical response of metastable austenitic steels. The simulations are compared with experimental mechanical and phase fraction data from different austenitic steels subjected to simple tension, plane strain tension, equibiaxial tension, simple compression, and torsion. It is demonstrated that the appropriate modeling of α'-martensite phase fractions allows capturing the experimentally measured mechanical response. The implementation and insights from these predictions, including the role of texture evolution on martensite transformation, are discussed in this paper.

1. Introduction

The high uniform elongation and hardening, and hence good formability of transformation-induced-plasticity (TRIP) steels with sufficiently low stacking fault energy (SFE), results from the deformation-induced austenite (face-centered cubic (fcc), γ-austenite) to martensite (body-centered tetragonal (bct), which is usually approximated as body-centered cubic (bcc), α'-marteniste) transformation. Martensite nucleation sites within austenite have been shown to be shear band intersections [1–4] and arise from stacking faults (SFs), ε-martensite (hexagonal close-packed (hcp)), mechanical twins [3], and slip bands [5]. The austenite phase may contain pre-existing nucleation sites which form during the thermomechanical processing of steels. These sites, which are the nucleation sites of thermally-induced martensite when the material is exposed to temperatures below the martensitic transformation (Ms) temperature, can also be activated in the very early stages of deformation. Transformation at pre-existing sites is referred to as stress-assisted [1,6]. When the materials deform plastically, new nucleation sites are introduced through the generation of new defects. The martensite forming at these sites is referred to as strain-induced [2,7–9]. The material properties and deformation conditions such as temperature, chemical composition, texture, load path and strain rate affect the rate of the strain-induced martensitic transformation [10–18].

The effect of chemical composition and temperature on the rate of the strain-induced martensitic transformation is linked to their influence on the SFE determining the stacking fault width (SFW), when a perfect dislocation dissociates into Shockley partials in fcc materials [3,19]. Under the influence of external stress, the SFW can

* Corresponding author. Department of Mechanical Engineering, University of New Hampshire, 33 Academic Way, Kingsbury Hall, W119, Durham, NH, 03824, USA.
E-mail address: marko.knezevic@unh.edu (M. Knezevic).

https://doi.org/10.1016/j.actamat.2018.12.060
1359-6454/

further increase resulting in the formation of shear bands. The presence of α'-martensite and shear bands alters the mechanical response of the materials due to the interaction of dislocations with martensite and bands [16]. Since α'-martensite is a harder phase than the austenite matrix, the onset of the transformation contributes to additional work hardening.

In the classical strain-induced austenite-to-martensite transformation kinetic model by Olson and Cohen [2], the evolution of the volume fraction of α'-martensite is a sigmoidal function of the macroscopic strain. This empirical model has served as a basis for many recent developments of kinetic models. More recent developments introduced scalar variables characterizing the stress state that affect the evolution of martensite: either just the stress triaxiality [8,20,21], or the stress triaxiality and the Lode angle parameter [11,12,14,22]. The effect of the stress triaxiality and Lode angle parameters is interpreted through the contribution of the mechanical driving force to the chemical driving force for the fcc to bcc transformation [8,12]. In all the above models, the relationship between martensite volume fraction and strain (or strain-rate) is characterized using stress-dependent fitting parameters, such as e.g. the α_θ and α_η in Ref. [12] or the n-parameter in Ref. [22], however, the obtained fits for these parameters have little physical meaning. Additionally, the role of microstructural phenomena such as the texture evolution and anisotropy, which affect the martensitic transformation, is not captured by any of these models.

In the above models, the loading path is only taken into account through the stress state parameters neglecting that the direction of deformation influences the SFW [23] and hence the shear band formation [3,24–27]. Recently, electron backscatter diffraction (EBSD) and in-situ neutron diffraction experiments showed that the suppression or facilitation of the martensitic transformation during the deformation of 201 steels is related to the changes in the SFW and the different resolved shear stresses experienced by the leading and trailing partial dislocations [4]. A recent study [28] implemented the classical kinetic model of Olson and Cohen in a crystal plasticity model which predicts the micromechanical response of polycrystalline materials. The combined model accounts for the role of texture and anisotropy on plastic strain of single crystals in a polycrystalline material, which furthermore influences the martensite evolution in each grain. However, the martensite evolution is purely dependent on the plastic strain and is independent from the stress state and crystal orientation, meaning that any two grains with similar plastic strain evolution will have similar martensite fraction evolution, which is inconsistent with experimental observations [4]. Therefore, the implementation is not capable of predicting the strain path dependence of martensitic transformation.

The objective of this study is to extend the classical kinetic model by Olson and Cohen [1] to (i) account for the effect of loading path on the number of potential nucleation sites for the strain-induced martensitic transformation, and (ii) to give it the appropriate physical basis required to use it at the microscopic scale i.e. at the grain-level. The proposed physics-based kinetic model is integrated into the EPSC crystal plasticity model proposed by Ref. [29] and further developed in Refs. [30–36]. The model explicitly accounts for the effect of the stress state at the crystal level, and the crystal orientation on the evolution of martensite fraction, making it suitable for the investigation of martensitic transformations not only under different stress states (e.g. equibiaxial tension vs. uniaxial tension etc.), but also under strain path changes, although not addressed in the examples of the present work. This is demonstrated by fitting the model to in-situ neutron diffraction experiments performed on a 304 stainless steel during multiaxial deformation. The model is further validated using experimental data for several austenitic steels subjected to monotonic deformation tests with different stress states and temperatures found in the literature.

The paper is organized in seven sections, including the introduction. Section 2 provides information on materials, mechanical tests and experimental procedures used in this study. The Olson-Cohen kinetic model and the proposed extension are described in section 3 and appendix A. Section 4 presents the coupling of the kinetic model with the EPSC model and the determination of α'-martensite crystal properties. The simulated evolution of the stress, texture and α'-martensite volume fraction with strain is compared with experiments in section 5. In section 6, modeling assumptions are discussed in connection with: (i) the effect of the load path and (ii) the crystal orientation on the strain-induced α'-martensite transformation and (iii) the accuracy of simulated mechanical response. The major conclusions from this work are summarized in section 7. We use a convention where "$\cdot$" and "$\otimes$" are the dot product and tensor product, respectively.

2. Material and experiments

The materials investigated in the present study include four austenitic steels denoted as: AS-1, AS-2, AS-3 and AS-4. The experimental data for AS-1 are provided in this study, while the rest of the experimental data is taken from literature. A summary of the literature source, materials, texture, chemical composition and experiments is presented in Tables 1–3.

The austenitic steel labeled AS-1 is an annealed AISI 304 stainless steel in the form of 8 mm thick plate. The as-received material exhibits approximately random texture and average grain size of 35 μm as shown in Fig. 1. The geometry employed for the study has been optimized by FE simulations and has been used in a previous study of 316L steel [37]. In situ neutron diffraction tests were carried out at the time-of-flight (ToF) instrument POLDI [38,39] of the Swiss neutron spallation source, SINQ which is equipped with a biaxial rig [37]. The in-plane strain was measured with a 2-camera digital image correlation (DIC) system (GOM, Aramis 5 M). Uniaxial and equibiaxial tensile tests were performed on cruciform-shaped samples with loading rate 40 N/s. The neutron diffraction measurements were performed at regular intervals by interrupting the loading and keeping the displacement fixed (allowing for some gauge stress relaxation during 300s waiting time before initiating the neutron measurements). The data was analyzed with the POLDI standard single peak fitting procedure implemented in the Mantid software [40]. The diffraction peaks are well described by Gaussian functions, yielding information on peak position, width and integrated intensity. The martensite intensity fraction, f_m, is calculated as follows:

$$f_m = \frac{I^M_{int}}{I^M_{int} + I^A_{int}} \tag{1}$$

where I^M_{int} and I^A_{int} are the integrated intensities of all the martensite and austenite reflections, respectively. The neutron diffraction measurements showed that at room temperature (RT = 293 K) under uniaxial tension no martensitic transformation occurs,

Table 1
The sources for experimental data used in the present study, nomenclature for austenitic steel studied in this work, and their initial textures.

	Source	Label	Initial texture
AS-1	This paper	304	Fig. 1b
AS-2	(Wang et al., 2016)	304	Fig. 2
AS-3	(Lebedev and Kosarchuk, 2000)	18Cr-10Ni	Random
AS-4	(DeMania, 1995)	304L	Rolling

Table 2
Chemical composition (wt. %) of austenitic steels considered in the present study. Fe balances the provided compositions.

	C	Cr	Ni	Si	Mo	Mn	Cu	Ti	V	S	P	N
AS-1	<0.08	17.5–20	8–11	<1		<2				<0.03	<0.045	
AS-2	0.08	19	9.25	0.75	0	2						
AS-3	0.07	15.4	12.3	0.43	1.91	1.45	0.12	0.41	0.05			
AS-4	0.022	18.37	9.31	0.42	0.35	1.39	0.39			0.002	0.021	0.042

Table 3
Applied deformation and temperature [K] for each material. The temperatures at which austenite-to-martensite transformation is observed are highlighted in bold and underlined.

	Simple tension (ST)	Equibiaxial tension (EBT)	Simple compression (SC)	Plane strain tension (PST)	Torsion
AS-1	293	**293**			
AS-2	**293** and 348				
AS-3	**77** and 293		**77**		**77**
AS-4	**233** and 293			**233** and 293	

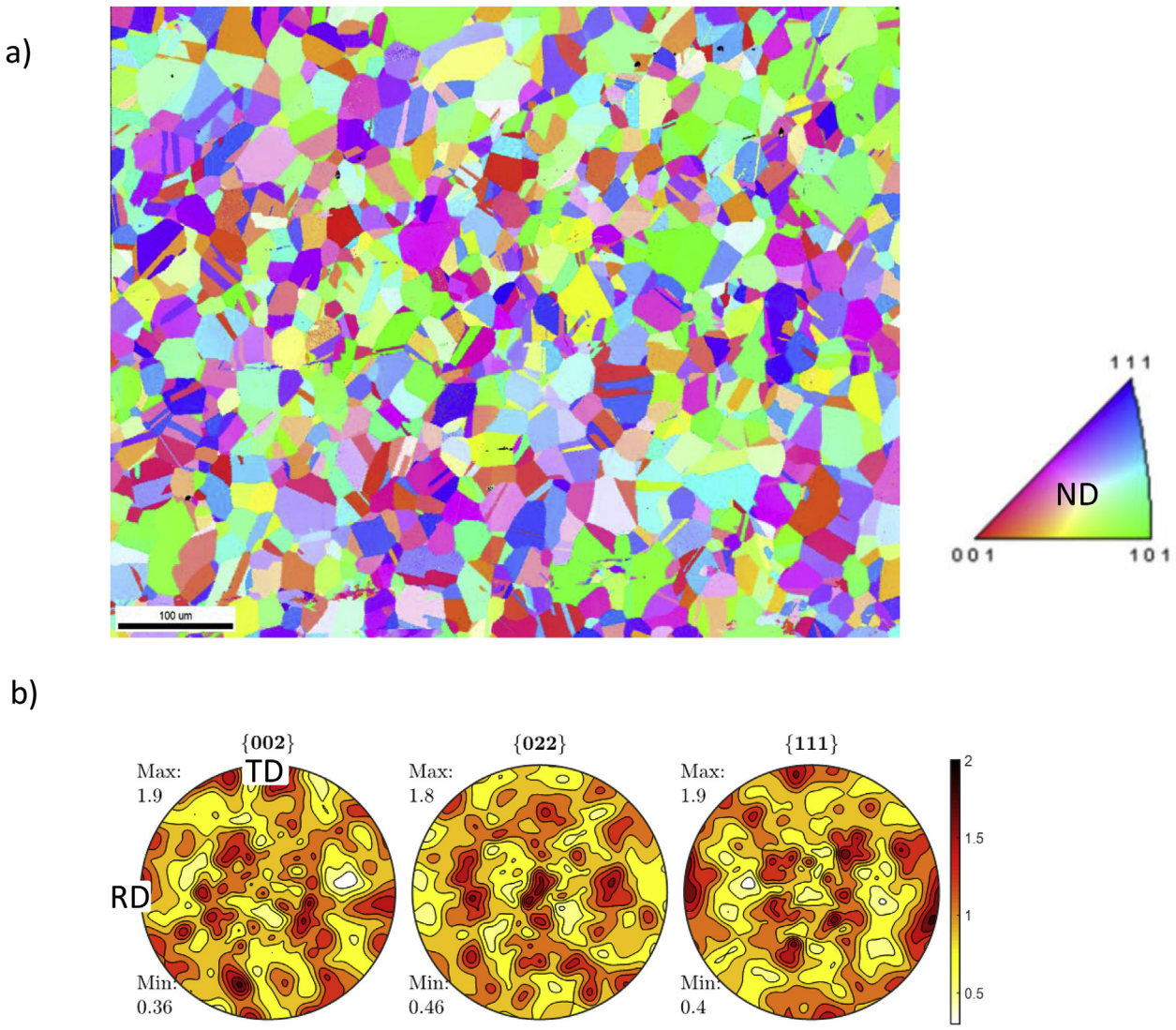

Fig. 1. (a) EBSD map and (b) stereographic pole figures showing the initial microstructure and texture in the austenitic steel 304, AS-1. The colors in the map in (a) indicate the crystal direction relative to the sample ND. (For interpretation of the references to color in this figure legend, the reader is referred to the Web version of this article.)

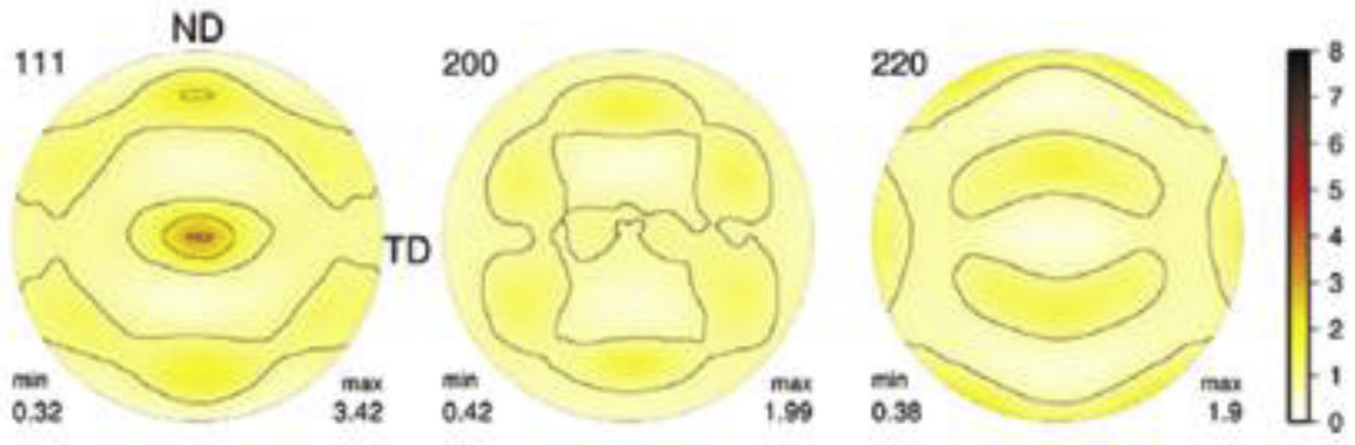

Fig. 2. Measured initial texture for AS-2 steel, taken from (Wang et al., 2016).

whereas martensite is formed under equibiaxial tension at RT. This is highlighted in Table 3.

The Initial texture for AS-2 is shown in Fig. 2 [28], whereas AS-3 and AS-4 have a random and rolling texture respectively, as mentioned in Table 1. AS-2, AS-3 and AS-4 were tested under different stress states and temperatures, as listed in Table 3. Table 3 also indicates the temperatures at which strain-induced martensite transformation occurs in these steels. Additional information on AS-2, AS-3 and AS-4 steels can be found in the provided references.

3. Strain induced austenite-to-martensite transformation kinetic model

3.1. The Olson-Cohen model

The strain-induced austenite to martensite transformation model proposed in Ref. [2] relates the total martensite volume fraction ($f^{\alpha'}$) to the macroscopic strain (ε):

$$f^{\alpha'} = 1 - \exp\{-\beta[1 - \exp(-\alpha\varepsilon)]^n\} \tag{2}$$

The parameter α represents the rate of shear-band formation and it increases with decreasing SFE and increasing strain rate. The parameter β is proportional to the probability that an intersection of shear bands will result in the nucleation of a martensite embryo. The parameter n is used to relate the number of shear band intersections with the volume fraction of shear bands and depends on the shear band geometry and orientation. Although the parameters (α, β, n) carry physically meaningful properties of the material, they are usually fit to the experimentally obtained total martensite fractions $f^{\alpha'}$ and the macroscopic strain ε [2]. Thus, the fitted parameters are averaged values of parameters dependent on the material properties, temperature, strain rate etc. To apply a kinetic model at the grain level, it needs to account for the microstructural aspects of the martensite formation and the mechanism of the transformation. As we will show, this can be achieved by modifying equation (2) of the model, applying the equation at the single crystal level and embedding it in a crystal plasticity framework.

3.2. Proposed extension of the Olson-Cohen model

The parameter set (α, β, n) varies not only with chemical composition and temperature, but also, as it will be shown, with the applied stress state and crystal orientation.

The general approach for introducing the load path, strain rate and temperature effects to the kinetic models, is to express the fitting parameters α and β as functions of load path, strain rate and temperature [12,20,41–44]. Inspired by the linear dependence of the fitting parameters with the triaxiality factor x_β suggested in Ref. [12], α is expressed as a linear function of the parameter x_α, which is related to the SFW. The stress state dependence in the Olson-Cohen model can then be written as:

$$\alpha = \alpha_0 + K_\alpha\, x_\alpha(\boldsymbol{\sigma}) \tag{3}$$

$$\beta = \beta_0 + K_\beta\, x_\beta(\boldsymbol{\sigma}) \tag{4}$$

where x_α and x_β are scalar parameters describing the stress state, while α_0, β_0, K_α and K_β are fitting parameters. If a combination of the fitting parameters and x_α and x_β produces $\alpha < 0$ and/or $\beta < 0$, the condition $\alpha = 0$ and/or $\beta = 0$ is enforced. The restrictions are coming from the definition of α and β parameters in the Olson-Cohen model. If $\alpha < 0$, the strain increments will produce negative increments of volume fraction of shear bands, which is physically not meaningful during monotonic loading. If $\beta < 0$, negative increments of volume fraction of α'-martensite will appear, which would imply reverse transformation from α'-martensite to austenite. The relation (4) describes how the stress state affects the probability that martensite will form at a shear band intersection. Therefore, the variables $x_\alpha(\boldsymbol{\sigma})$ and $x_\beta(\boldsymbol{\sigma})$ extract important information from the stress state, relevant to the shear band formation (the number of potential nucleation cites) and the subsequent martensite nucleation (the actual structural transformation at available nucleation cites). Since α and β are functions of the chemical composition and temperature [2], α_0, β_0, K_α and K_β are also dependent on the chemical composition and temperature. The strain rate affects the phase transformation through temperature increase originating from adiabatic heating [45]. Hence the strain rate dependence of parameters α_0, β_0, K_α and K_β is included in their temperature dependence, provided that adiabatic heating is accounted for by the model. In the derivation of variables $x_\alpha(\boldsymbol{\sigma})$ and $x_\beta(\boldsymbol{\sigma})$ it is assumed that $K_\alpha > 0$ and $K_\beta > 0$, while there is no restriction on the values of α_0 and β_0. The $K_\alpha > 0$ and $K_\beta > 0$ assumptions are arbitrary, stating that grains with higher $x_\alpha(\boldsymbol{\sigma})$ and $x_\beta(\boldsymbol{\sigma})$ should have higher α and β, and in turn more shear bands and more α'-martensite, respectively.

The shear band formation process per slip system is related to the separation distance between the leading and trailing partial

dislocations of that slip system, i.e. the SFW [3,26]. The SFW depends on the applied forces acting on the partial dislocations, the SFE and the elastic properties of the material. Such stacking faults including only one (111) plane are called intrinsic. However, dissociation on one (111) plane can trigger dissociation on neighboring (111) planes, causing thickening of the fault [46]. The presence of intrinsic SFs on every second (111) plane results in ε-martensite formation, while in the case of mechanical twin formation, the SFs are present on every (111). Both ε-martensite and mechanical twins can be treated as thick faults. The derived expression for the SFW of a thick fault on an active slip system is:

$$d = c(\mu,\ \nu,\ \theta,\ b_p)N^2 \Big/ \left[2\gamma_N - Nb_p\left(\left(\widehat{\mathbf{b}}_l - \widehat{\mathbf{b}}_r\right)\boldsymbol{\sigma}^c\right)\cdot\widehat{\mathbf{n}}\right] \tag{5}$$

where $\boldsymbol{\sigma}^c$ is the stress tensor of a grain, μ is the shear modulus, ν is the Poisson's ratio, θ is the angle between the dislocation line and the Burgers vector, γ_N is the fault energy, N is the number of intrinsic SFs in the fault i.e. number of the partial dislocations bounding the fault, $\widehat{\mathbf{b}}_l, \widehat{\mathbf{b}}_r$ are unit vectors in the Burgers direction of the left and right partial (see Appendix A for the terms left/right partial dislocation), $\widehat{\mathbf{n}}$ is the slip plane normal, $b_p = \frac{a}{\sqrt{6}}$ is the magnitude of the Burgers vector of the partial dislocation, and $c(\mu, \nu, \theta, b_p)$ is a constant defined in Appendix A with Eq. (A8) in terms of elastic properties (μ and ν), dislocation character (θ) and magnitude of the Burgers vector of the partial dislocation (b_p). The derivation of the expression for the SFW and the determination of partials for each slip system is also presented in appendix A. From Eq. (5), the SFW of intrinsic SFs can be retrieved by setting: $N = 1$ and $\gamma_N = \gamma$, where γ is the intrinsic SFE. The fault energy, γ_N, consists of the volume and surface components. The surface component of the fault energy is the free energy per unit area of the austenite/martensite interface [19]. If the intrinsic SFE is lower than the surface energy, the volume energy is negative and the formation of ε-martensite is favored [3]. In this case, γ_N decreases with increasing the number of intrinsic SFs in the fault, N. On the other hand, if the intrinsic SFE is higher than the surface energy, the formation of a mechanical twin is favored and the volume energy disappears since the mechanical twin has the same structure as austenite [3]. In this case, γ_N is constant and equal to two times the surface energy. From Eq. (5) it is apparent that increasing the fault thickness, N, results in widening of the SFW.

It is assumed that a shear band nucleates when the SFW tends to infinity [3,26]. According to Eq. (5), this happens when the denominator tends to zero. Therefore, the condition for the formation of a shear band on a slip system s is:

$$2\frac{\gamma_N}{N} - b_p\left(\left(\widehat{\mathbf{b}}_l^s - \widehat{\mathbf{b}}_r^s\right)\boldsymbol{\sigma}^c\right)\cdot\widehat{\mathbf{n}}^s = 0 \tag{6}$$

The stress state affects the process of shear band formation through the term: $((\widehat{\mathbf{b}}_l^s - \widehat{\mathbf{b}}_r^s)\boldsymbol{\sigma}^c)\cdot\widehat{\mathbf{n}}^s$. The expression for the scalar variable $x_\alpha(\boldsymbol{\sigma})$, extracting only the stress state effect on the shear band formation from a stress tensor, is:

$$x_\alpha = \sum_s \frac{\left(\left(\widehat{\mathbf{b}}_l^s - \widehat{\mathbf{b}}_r^s\right)\boldsymbol{\sigma}^c\right)\cdot\widehat{\mathbf{n}}^s}{|\boldsymbol{\sigma}^c\cdot\mathbf{m}^s| n_{act}} \tag{7}$$

where the sum goes over all the active slip systems, n_{act} is the number of all the active slip systems, and $\mathbf{m}^s$ is the Schmid tensor. Equation (7) defines a scalar parameter x_α that is large for stress states that promote shear band formation, and low for stress states that inhibit shear band formation. The greater the $((\widehat{\mathbf{b}}_l^s - \widehat{\mathbf{b}}_r^s)\boldsymbol{\sigma}^c)\cdot\widehat{\mathbf{n}}^s$ term, the greater the SFW, which can be related to the formation of extended shear bands acting as potential nucleation sites. To exclude the stress magnitude effect from the parameter x_α, the expression is normalized with the resolved shear stress, $|\boldsymbol{\sigma}^c\cdot\mathbf{m}^s|$. The average value of the ratio $\frac{((\widehat{\mathbf{b}}_l^s - \widehat{\mathbf{b}}_r^s)\boldsymbol{\sigma}^c)\cdot\widehat{\mathbf{n}}^s}{|\boldsymbol{\sigma}^c\cdot\mathbf{m}^s|}$ is taken over the active slip systems within a grain. For a given stress state described with the stress tensor, $\boldsymbol{\sigma}^c$, the set of active slip systems and the directions of the Burgers vectors of the partial dislocations, $\widehat{\mathbf{b}}_l^s$ and $\widehat{\mathbf{b}}_r^s$, and the slip plane normal, $\widehat{\mathbf{n}}^s$, depend on the crystal orientation. Therefore, the x_α parameter accounts for the crystallographic effects.

The probability of nucleation of martensite at a shear band intersection is proportional to the stress triaxiality via the dependence of the potency distribution function to the stress state [8,20]. In their original model, Olson and Cohen have assumed that each nucleation site has its own critical driving force, i.e. potency. The transformation at a given nucleation site occurs once the summation of the chemical and the mechanical driving forces reaches this critical value. The chemical driving force is the difference in Gibbs free energies between austenite and α'-martensite and it depends on temperature [47], while the critical driving force is the difference in Gibbs free energies between austenite and α'-martensite at the temperature at which the thermal transformation occurs spontaneously (i.e. without application of external mechanical force). The mechanical driving force is the work density performed by or on the transformed volume [48]. Physically, the mechanical contribution to the thermodynamic driving force, is perceived as the interaction of the stress state with the strain of the transformation, to increase or decrease the potency (hence the probability) for nucleation at a given nucleation site [48]. The shear part of transformation strain is accommodated by shear bands forming the nucleation site. Consequently, the stress state is only interacting with the volumetric strain of the transformation. The scalar variable $x_\beta(\boldsymbol{\sigma})$, which is related to the probability of martensite nucleation, is therefore:

$$x_\beta = -\frac{p}{\sigma^{eq}} \tag{8}$$

where $p = -\frac{1}{3}tr\ \boldsymbol{\sigma}$ is the hydrostatic pressure and σ^{eq} is the von Mises equivalent stress. For a given stress state, $\boldsymbol{\sigma}^c$, of a crystal, the stress triaxiality is defined without any dependence to the crystal orientation. Hence, the parameter x_β is considered independent to the crystal orientation.

4. Implementing the kinetic model in the EPSC model

4.1. Formation and evolution of martensitic phase

The transformation starts when the stress reaches a critical value that causes the SFW to expand to infinity [26], as shown in Eq. (6). Evidently, the key variables for the onset of the transformation are the stress magnitude and the SFE.

The evolution of martensite is suppressed in the model until the condition of Eq. (6) is fulfilled for at least one grain in the polycrystal. The EPSC model predicts only the average stress value per crystal and does not account for the intragranular stress distribution inside the grains, while in reality the condition of Eq. (6) can be fulfilled locally even if the average stress in the grain does not fulfill the condition. Nevertheless, the onset of the transformation is the same for all grains, while the propensity of transformation will be different for each grain depending on its stress state and orientation. Once the condition is fulfilled, the martensite evolution is governed by the Olson-Cohen kinetic model at the single crystal level in the incremental form. The incremental form of Eq. (2) is:

$$df^{\alpha'} = \left(1 - f^{\alpha'}\right)\beta n\left(f^{sb}\right)^{n-1} df^{sb} \tag{9a}$$

$$df^{sb} = \alpha\left(1 - f^{sb}\right)d\varepsilon \tag{9b}$$

where f^{sb} is the volume fraction of shear bands. The incremental form is necessary since parameters α and β now vary during the evolution of shear strain and analytical integration of Eqs. (9a) and (9b) is no longer possible. The single crystal analogue of Eq. (9) is:

$$dw^{c,m} = \left(w_0^c - w^{c,m}\right)\beta n\left(f^{c,sb}\right)^{n-1} df^{c,sb} \tag{10a}$$

$$df^{c,sb} = \alpha\left(1 - f^{c,sb}\right)\sum_s d\gamma^s \tag{10b}$$

where w_0^c is the initial volume fraction of the parent austenite grain, $w^{c,m}$ is the volume fraction of the product, martensite, grain. The use of sum of shear strains on slip systems, $\sum d\gamma^s$, in the single crystal version of the Olson-Cohen law has been suggested in Ref. [28].

Using Eqs. (6) and (10) for all crystals, it is assumed that potentially each crystal can undergo strain-induced martensitic transformation. In the materials studied here the transformation becomes apparent during plastic deformation, hence the strain-induced transformation is the dominant mechanism [7]. Any transformation mechanism other than the theory presented in Ref. [2] is not considered in the present study.

The volume fraction of martensite for each austenite crystal evolves as a function of shear strain and stress state per crystal using Eq. (10). Once the volume fraction of martensite reaches 1% of parent austenite grain, a new grain is created and added to the polycrystalline aggregate. Due to the presence of cubic symmetry, 24 possible martensite variants can be nucleated from one grain of austenite. Each variant has a specific crystallographic relationship with its parent austenite grain and corresponding phase transformation strain, see Refs. [28,43]. Only one martensite variant is assumed to nucleate from one austenite grain, which agrees with experimental observations for the majority of the investigated grains by EBSD [5]. More details on the orientation determination procedure and calculation of phase transformation strain is presented in appendix B.

After an increment in time, dt, the strain increment of the transformed volume $dw^{c,m}$ is $\boldsymbol{\varepsilon}^{pt,i}$ (Fig. 3) and in Ref. [28] the phase transformation strain is added only to the austenite parent grain. In the present study the phase transformation strain of the transforming volume, $dw^{c,m}$, is averaged over the volume of austenite and martensite grains and assigned as a transformation strain for both austenite and martensite grains:

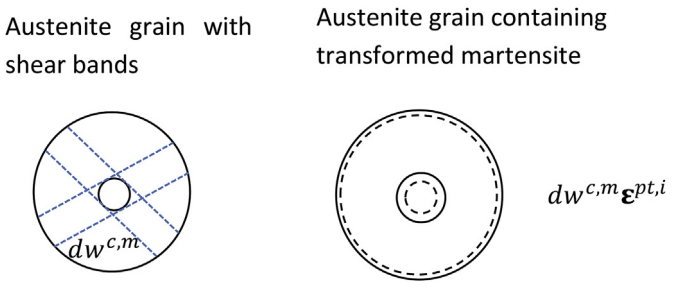

Fig. 3. An austenite grain represented with a sphere before and after martensitic transformation of volume $dw^{c,m}$

$$\dot{\boldsymbol{\varepsilon}}^{pt,a} = \dot{\boldsymbol{\varepsilon}}^{pt,m} = \frac{\dot{w}^{c,m}\boldsymbol{\varepsilon}^{pt,i}}{w^{c,a} + w^{c,m}} \tag{11}$$

where $\dot{\boldsymbol{\varepsilon}}^{pt,a}$, $\dot{\boldsymbol{\varepsilon}}^{pt,m}$, $w^{c,m}$ and $w^{c,a}$ are the rate of phase transformation strain in the austenite and martensite grains and the volume fractions of austenite and martensite grains, respectively.

The stress and strain of the transformed martensite volume increment, $dw^{c,m}$, need to be defined. The first increment in martensite volume fraction is assigned the stress of the austenite matrix. Due to the very small initial volume fraction of martensite, this initial assumption for the stress of martensite is not critical for the predictions of the mechanical response. Since martensite has higher slip resistance than austenite, martensite starts deforming elastically and the stress increases with further straining. Upon increasing the martensite fraction, each next increment in martensite volume fraction is assigned the same stress as the already formed martensite grain. This assumption was adopted in an earlier study reported in Ref. [28], where a similar mean-field model was used to simulate the lattice strains in martensite and austenite phases. Since capturing the evolution of lattice strain, in both phases, is outside the scope of the present work, this assumption is sufficient for capturing the evolution of martensite and the macroscopic mechanical behavior of the material.

The strain of the martensite volume increment is defined based on the non-elastic strain in austenite and the stress of the product martensite grain. The total shape change is described by the non-elastic strain, while the deformation of the actual lattice is described with the total elastic strain coming from the total stress. The shape change due to the non-elastic deformation is not reversible and has already happened in the region that is to become martensite. Any transformation of the lattice does not change this fact, nor does it remove the already present strain in this region. Therefore, the total non-elastic strain of the currently transforming volume is equal to that of the parent grain and the total strain is:

$$\boldsymbol{\varepsilon}^{dm} = \boldsymbol{\varepsilon}^{ne,a} + \boldsymbol{\varepsilon}^{el,dm} \tag{12}$$

where $\boldsymbol{\varepsilon}^{dm}$ is the total strain in the transformed martensite volume increment, $\boldsymbol{\varepsilon}^{ne,a}$ is the total non-elastic strain in the austenite grain and $\boldsymbol{\varepsilon}^{el,dm}$ is the total elastic strain in the transformed volume increment. The elastic strain of the transformed volume is calculated from the stress in the martensite grain. Therefore, the strain of the updated martensite grain containing the transforming volume increment is:

$$\boldsymbol{\varepsilon}^{m+dm} = \frac{\left(\boldsymbol{\varepsilon}^{m} w^{c,m} + \boldsymbol{\varepsilon}^{dm} dw^{c,m}\right)}{w^{c,m} + dw^{c,m}}. \tag{13}$$

The initial slip resistance and the parameters governing the evolution of slip resistance are fit parameters obtained by fitting the experimental mechanical data.

4.2. EPSC equations accommodating the extended phase transformation kinetic model

The description of the elasto-plastic self-consistent (EPSC) modeling framework can be found in Refs. [29,30]. To model the phase transformation, the phase transformation strain rate is introduced into the single crystal constitutive relation:

$$\hat{\boldsymbol{\sigma}}^c = \mathbf{C}^c\left(\dot{\boldsymbol{\varepsilon}}^c - \dot{\boldsymbol{\varepsilon}}^{pl,c} - \dot{\boldsymbol{\varepsilon}}^{pt,c}\right) - \boldsymbol{\sigma}^c tr(\dot{\boldsymbol{\varepsilon}}^c) \tag{14}$$

where $\hat{\boldsymbol{\sigma}}^c$ is the Jaumann stress rate, $\mathbf{C}^c$ is the fourth rank elastic stiffness tensor, $\dot{\boldsymbol{\varepsilon}}^c$ is the total strain rate, $\dot{\boldsymbol{\varepsilon}}^{pl,c}$ is the plastic strain rate

and $\dot{\boldsymbol{\varepsilon}}^{pt,c}$ is the phase transformation strain rate. Note that the total strain rate consists from the elastic, plastic and phase transformation strain rate. The single crystal constitutive relation can be expressed in the following form:

$$\widehat{\boldsymbol{\sigma}}^{c} = \mathbf{L}^{c}\left(\dot{\boldsymbol{\varepsilon}}^{c} - \dot{\boldsymbol{\varepsilon}}^{pt,c}\right) \tag{15}$$

where $\mathbf{L}^{c}$ is the instantaneous elasto-plastic stiffness. $\mathbf{L}^{c}$ is formed based on the adopted slip resistance evolution with the shear strain on the slip systems i.e. the hardening law. The hardening law used here is developed in Refs. [31,49]. The reader is referred to Ref. [31] for detailed description of the hardening law and hardening parameters calibrated in this work. Note that the transformation-induced back-stress is not simulated in this work as in Ref. [28]. A similar relationship is adopted for the overall polycrystalline aggregate:

$$\widehat{\boldsymbol{\sigma}} = \mathbf{L}\left(\dot{\boldsymbol{\varepsilon}} - \dot{\boldsymbol{\varepsilon}}^{pt}\right) \tag{16}$$

where $\widehat{\boldsymbol{\sigma}}$, $\dot{\boldsymbol{\varepsilon}}$ and $\dot{\boldsymbol{\varepsilon}}^{pt}$ are the Jaumann stress rate, the total strain rate and the phase transformation strain rate of the polycrystalline aggregate, respectively. $\mathbf{L}$ is the instantaneous elasto-plastic stiffness of the homogenized polycrystalline aggregate. Analogues to single crystal, the total strain rate of the polycrystalline aggregate consists from the elastic, plastic and phase transformation strain rate. $\mathbf{L}$ and $\dot{\boldsymbol{\varepsilon}}^{pt}$ are unknown and are evaluated using the self-consistent homogenization scheme [31,50]. The deviation of a crystal stress rate from the stress rate of the polycrystalline aggregate is proportional to the corresponding strain rate deviation, through the interaction tensor,$\mathbf{L}^{*}$:

$$\widehat{\boldsymbol{\sigma}}^{c} - \widehat{\boldsymbol{\sigma}} = -\mathbf{L}^{*}\left(\dot{\boldsymbol{\varepsilon}}^{c} - \dot{\boldsymbol{\varepsilon}}\right) \tag{17}$$

The interaction tensor is defined in terms of the Eshelby tensor, $\mathbf{S}^{c}$, as: $\mathbf{L}^{*} = \mathbf{L}(\mathbf{S}^{c^{-1}} - \mathbf{I})$. Combining Eqs. (15)–(17) produces:

$$\mathbf{L}^{c}\left(\dot{\boldsymbol{\varepsilon}}^{c} - \dot{\boldsymbol{\varepsilon}}^{pt,c}\right) - \mathbf{L}\left(\dot{\boldsymbol{\varepsilon}} - \dot{\boldsymbol{\varepsilon}}^{pt}\right) = -\mathbf{L}^{*}\left(\dot{\boldsymbol{\varepsilon}}^{c} - \dot{\boldsymbol{\varepsilon}}\right) \tag{18}$$

From Eq. (18), the single crystal strain rate can be expressed in terms of the unknown reference strain rate [51]:

$$\dot{\boldsymbol{\varepsilon}}^{c} = \mathbf{A}^{c}\dot{\boldsymbol{\varepsilon}}^{ref} + \mathbf{a}^{c} \tag{19}$$

with:

$$\mathbf{A}^{c} = \left(\mathbf{L}^{c} + \mathbf{L}^{*}\right)^{-1}\left(\mathbf{L} + \mathbf{L}^{*}\right) \tag{20}$$

$$\mathbf{a}^{c} = \left(\mathbf{L}^{c} + \mathbf{L}^{*}\right)^{-1}\left(\mathbf{L}^{c}\dot{\boldsymbol{\varepsilon}}^{pt,c} - \mathbf{L}\dot{\boldsymbol{\varepsilon}}^{pt}\right) \tag{21}$$

where $\dot{\boldsymbol{\varepsilon}}^{ref}$ is the reference strain rate. Equating the volume average of the single crystal strain rates to the strain rate of the polycrystalline aggregate allows the evaluation of the reference strain rate:

$$\dot{\boldsymbol{\varepsilon}}^{ref} = \langle\mathbf{A}^{c}\rangle^{-1}\dot{\boldsymbol{\varepsilon}} - \langle\mathbf{A}^{c}\rangle^{-1}\langle\mathbf{a}^{c}\rangle \tag{22}$$

The condition that the volume average of the single crystal stress rates is equal to the stress rate of the polycrystalline aggregate yields:

$$\widehat{\boldsymbol{\sigma}} = \langle\mathbf{L}^{c}\mathbf{A}^{c}\rangle\langle\mathbf{A}^{c}\rangle^{-1}\dot{\boldsymbol{\varepsilon}} - \langle\mathbf{L}^{c}\mathbf{A}^{c}\rangle\langle\mathbf{A}^{c}\rangle^{-1}\langle\mathbf{a}^{c}\rangle + \left\langle\mathbf{L}^{c}\left(\mathbf{a}^{c} - \dot{\boldsymbol{\varepsilon}}^{pt,c}\right)\right\rangle \tag{23}$$

The macroscopic instantaneous elasto-plastic stiffness and the phase transformation strain rate are identified by the comparison of Eqs. (16) and (23):

$$\mathbf{L} = \langle\mathbf{L}^{c}\mathbf{A}^{c}\rangle\langle\mathbf{A}^{c}\rangle^{-1} \tag{24}$$

$$\dot{\boldsymbol{\varepsilon}}^{pt} = \langle\mathbf{a}^{c}\rangle - \mathbf{L}^{-1}\left\langle\mathbf{L}^{c}\left(\mathbf{a}^{c} - \dot{\boldsymbol{\varepsilon}}^{pt,c}\right)\right\rangle. \tag{25}$$

4.3. Simulation setups

The input for the EPSC model includes the starting texture, the single crystal elastic constants, the set of all possible slip systems and the initial grain shapes. In addition, the parameters of the hardening law and of the kinetic model need to be calibrated by comparing the simulated and measured mechanical responses and the martensite fractions respectively, as described in the subsequent section.

The initial texture for the AS-1 material is shown in Fig. 1b. A rolling texture, consisting of 500 weighted crystal orientations, is generated using the MTEX software [52] and it is used as the starting texture for the AS-2 material. The same texture is also used for the AS-4 material since [53] reports an initial rolling texture. For AS-3, the initial texture is assumed to be random.

The single crystal elastic constants for austenite are $C_{11} = 209\ GPa$, $C_{12} = 133\ GPa$ and $C_{44} = 121\ GPa$, while the single crystal elastic constants for martensite are $C_{11} = 234\ GPa$, $C_{12} = 135\ GPa$ and $C_{44} = 118\ GPa$ [28]. The $\left\{1\bar{1}1\right\}\langle 110\rangle$ and the $\{110\}\left\langle 1\bar{1}1\right\rangle$ slip systems are used for austenite and martensite respectively. Each grain in the EPSC model is set to be a spherical inhomogeneity in the effective medium at the beginning of deformation and evolves into an ellipsoid during deformation.

Appropriate boundary conditions are used to simulate the applied stress states: simple tension and compression, equibiaxial tension, torsion and plane strain tension. The simple tension/compression is simulated by imposing normal strain increments in the tensile/compressive direction, while enforcing the normal stresses in the lateral directions and all the shear strains to be zero. The equibiaxial tension of material AS-1 was simulated by imposing the experimental strain history for the two normal strain components along the in-plane loading directions (RD and TD). All the shear strain components and the out-of-plane normal stress component were enforced to be zero. To simulate the torsion deformation of the AS-3 material, plane stress state in the plane containing 1 and 2 directions is imposed, while imposing shear strain increments, $\Delta\varepsilon_{12}$, and keeping normal strains in directions 1 and 2 at zero. The plane strain tension of the AS-4 material is imposed by applying strain increments along RD, while enforcing the normal strain along TD, and all the shear strains and normal stress along ND, to be zero.

The non-elastic strain rate in the model is:

$$\dot{\boldsymbol{\varepsilon}}^{ne} = \frac{\left\langle\boldsymbol{\varepsilon}^{c}_{t+\Delta t}\right\rangle - \left\langle\mathbf{S}^{c}_{t+\Delta t}\boldsymbol{\sigma}^{c}_{t+\Delta t}\right\rangle - \left(\left\langle\boldsymbol{\varepsilon}^{\mathbf{c}}_{t}\right\rangle - \left\langle\mathbf{S}^{c}_{t}\boldsymbol{\sigma}^{c}_{t}\right\rangle\right)}{\Delta t} \tag{26}$$

where $\mathbf{S}^{c}$ is the elastic compliance of crystal c. The equivalent non-elastic strain is then defined as: $\varepsilon^{eq} = \int_{0}^{t}\dot{\varepsilon}^{eq,ne}dt$, with $\dot{\varepsilon}^{eq} = \sqrt{\frac{2}{3}\dot{\boldsymbol{\varepsilon}}^{ne}\cdot\dot{\boldsymbol{\varepsilon}}^{ne}}$. The non-elastic strain contains both the plastic and the transformation strain. It is comparable with the equivalent plastic strain used to plot the experimental results for steels AS-3 and AS-4.

5. Results

The EPSC model, implemented with the proposed strain-

induced austenite-to-martensite transformation kinetic model, is applied to simulate the mechanical and microstructural response of four austenitic steels, including their stress-strain response and texture evolution. The stress state and the temperature are varied, resulting in different measured stress-strain responses and martensite fractions. The loading is quasi-static and therefore the strain-rate effect on the phase transformation is not considered.

Figs. 4 and 5 show, respectively, for AS-1, AS-2, AS-3 and AS-4 the comparisons between the simulated and measured stress-strain responses and the volume fractions of α'-martensite. The calibration of austenite and martensite phase hardening parameters and the kinetic model parameters is performed in three steps. First, the austenite phase hardening parameters are obtained by fitting the experimental stress-strain curves at loads/temperatures where martensite does not form, i.e. simple tension at 293 K for AS-1 (Fig. 4a), simple tension at 348 K for AS-2 (Fig. 4b), simple tension at 293 K for AS-3 (Fig. 4c) and simple tension at 293 K for AS-4 (Fig. 4d). The calibrated hardening law parameters for the austenite phase are shown in Table 4. The parameters related to slip system interactions (L^{ss}, $L^{ss'}$, g^{ss}, $g^{ss'}$), the debris dislocation density evolution (q), and the drag stress (D) were selected based on previous works and, thus, were not altered during the fitting procedure. In contrast, the initial slip resistance (τ_0), the coefficient governing the rate of generation of dislocations (k_1), and the activation energy (g) were changed to fit the stress stain curves. The initial slip resistance for austenite at other temperatures, where martensite forms, is also reported in Table 4. The initial slip resistance at these temperatures was calibrated by comparing the simulated and measured yield stresses. Plastic deformation by slip in austenite always precedes martensite formation and hence, the yield stress is determined by austenite slip resistance only.

Second, the kinetic model parameters (shown in Table 6) are obtained by fitting the measured values of the martensite volume fraction shown in Fig. 5. For each material, the phase transformation occurs only at one temperature: 293 K for AS-1 (Fig. 5a) and AS-2 (Figs. 5b), 77 K for AS-3 (Figs. 5c), and 233 K for AS-4 (Fig. 5d). Note that the β_0 parameter for AS-1 is set to negative in order to suppress the phase transformation during simple tension

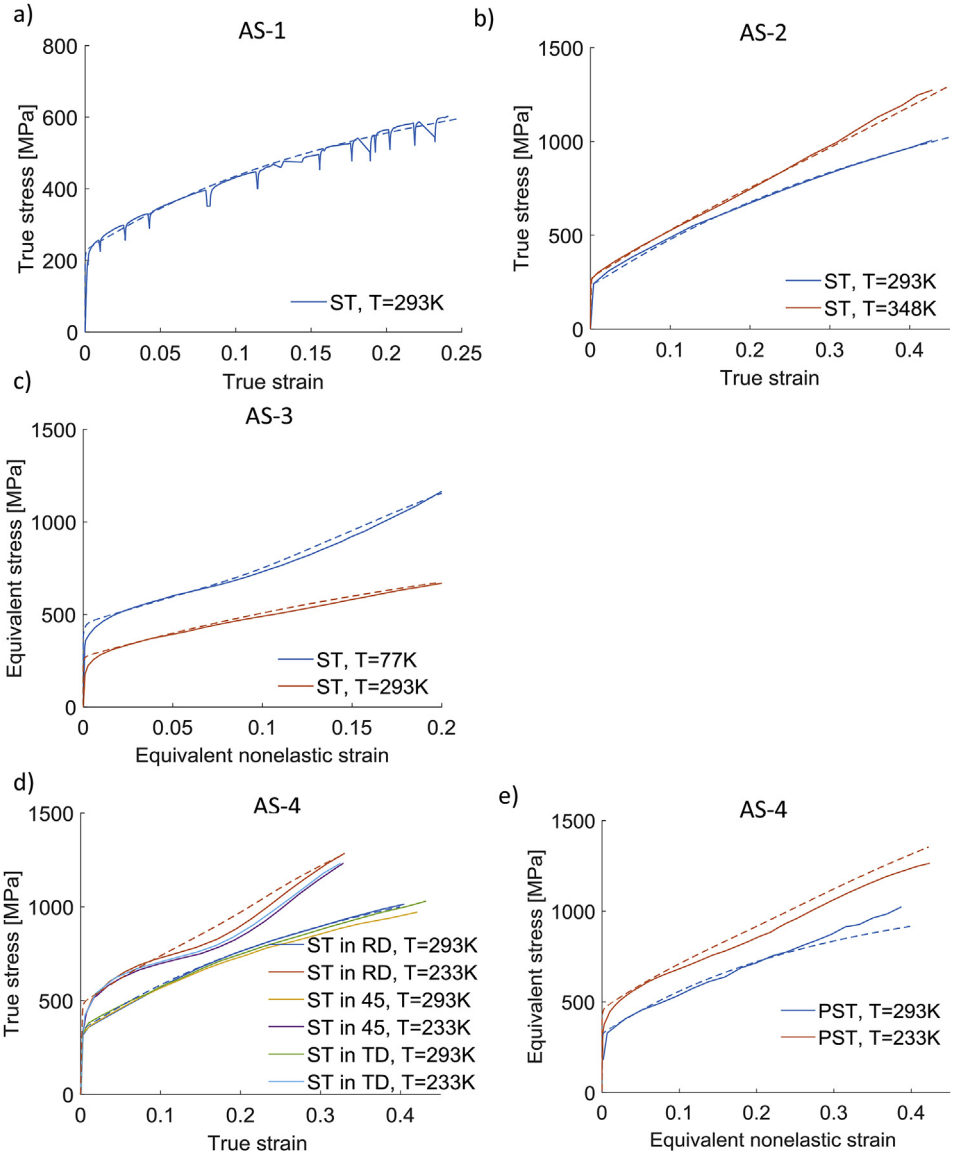

Fig. 4. Comparison of the simulated (dashed lines) and measured (full lines) mechanical response for (a) simple tension (ST) stress-strain curves at room temperature for AS-1, (b) ST stress-strain curves at 293 K and 348 K for AS-2, (c) ST stress-strain curves at 77 K and 293 K for AS-3, (d) ST stress-strain curves at 233 K and 293 K for AS-4 and (e) stress-strain curves at 233 K and 293 K for plane strain tension (PST) in RD for AS-4.

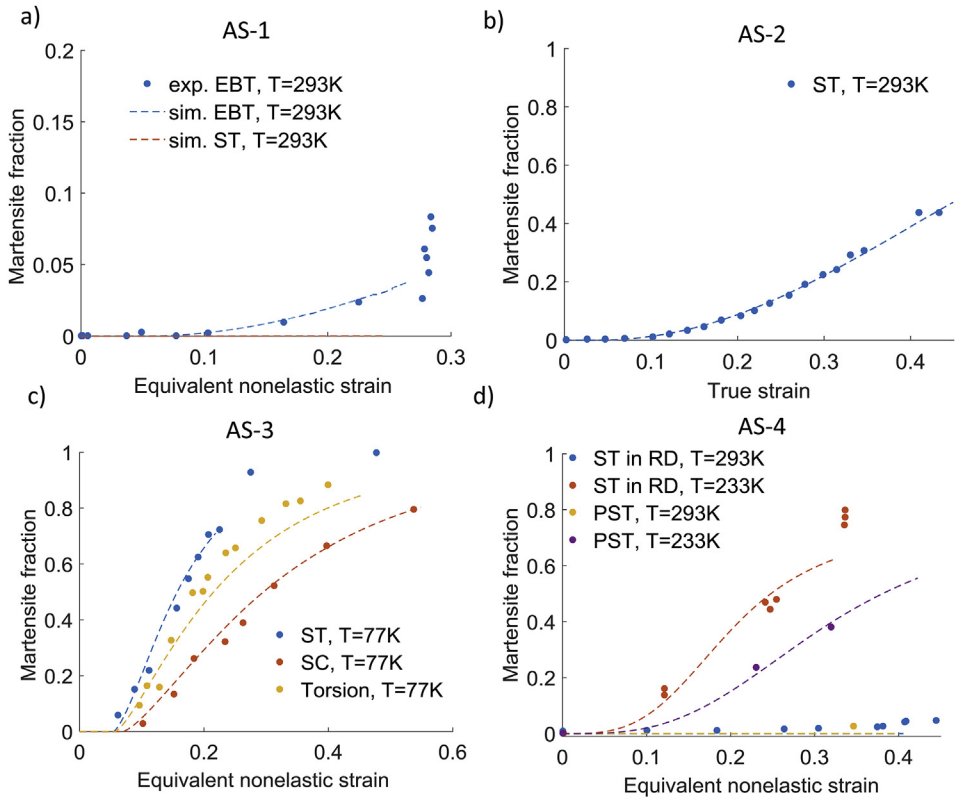

Fig. 5. Comparison of the simulated and measured martensite fraction for (a) equibiaxial tension (EBT) at room temperature (293 K) for AS-1, (b) ST at room temperature (293 K) for AS-2, (c) ST, simple compression (SC) and torsion at 77 K for AS-3 and (d) ST and PST in RD at 233 K and 293 K for AS-4.

Table 4
Hardening law parameters for austenite.

Material	Loading state/Temperature	L^{ss}	$L^{ss'}$	g^{ss}	$g^{ss'}$	τ_0[MPa]	$k_1[m^{-1}]$	g	D[MPa]	q
AS-1	ST/293K	1	1	1	0	64	0.95×10^8	0.09	100	8
AS-2	ST/348K	1	1	1	0	65 @ 348K 80 @ 293K	0.92×10^8	0.24	100	8
AS-3	ST/293K	1	1	1	0	80 @ 293K 145 @ 77K	0.92×10^8	0.15	100	8
AS-4	ST/293K	1	1	1	0	105 @ 293K 155 @ 233K	0.92×10^8	0.16	100	8

Table 5
Hardening law parameters for martensite.

Material	Loading state/Temperature	L^{ss}	$L^{ss'}$	g^{ss}	$g^{ss'}$	τ_0[MPa]	$k_1[m^{-1}]$	g	D[MPa]	q
AS-1	Taken from AS-2	1	1	1	0	280 @ 293K	1×10^8	0.25	100	8
AS-2	ST/293K	1	1	1	0	350 @ 293K	1×10^8	0.25	100	8
AS-3	ST/77K	1	1	1	0	260 @ 77K	1×10^8	0.25	100	8
AS-4	ST/233K	1	1	1	0	280 @ 233K	1×10^8	0.25	100	8

while fitting the measured α'-martensite fraction during equibiaxial tension. Suppressing the transformation for simple tension reduces to condition: $\beta_0 + K_\beta x_\beta(\boldsymbol{\sigma}^{ST}) \leq 0$, while in order to get the transformation during EBT, the condition: $\beta_0 + K_\beta x_\beta(\boldsymbol{\sigma}^{EBT}) > 0$ is valid. From the two conditions and using $x_\beta(\boldsymbol{\sigma}^{ST}) = \frac{1}{3}$ and $x_\beta(\boldsymbol{\sigma}^{EBT}) = \frac{2}{3}$ we get: $-\frac{1}{3}K_\beta \geq \beta_0 > -\frac{2}{3}K_\beta$. Since we assume $K_\beta > 0$, it follows that $\beta_0 < 0$. Physically this can be interpreted as lack of sufficient mechanical driving force to cause the transformation at the nucleation sites during uniaxial tension (see section 3.2). The exponent, n, for all materials in the present study is set as a fit parameter, as opposed to the original work of Olson and Cohen, and similar studies, where it is fixed to the value of 4.5 [2,45,54]. In the present study, the obtained values of the exponent n are lower than the established value of 4.5, that according to Ref. [2], represents a low number of non-random distribution of shear bands that rapidly increase by straining. The relatively small value of n, in the present

Table 6
Kinetic model parameters.

Material	α_0	K_α	β_0	K_β	n	$\frac{\gamma_N}{N}\left[\frac{mJ}{m^{-2}}\right]$	$T[K]$
AS-1	0.28	0.0	−4.0	10.0	2.0	5.0	293K
AS-2	0.25	0.0	12.0	0.0	2.15	5.5	293K
AS-3	0.62	0.45	6.0	4.0	1.4	9.3	77K
AS-4	0.6	1.9	5.0	5.0	4.0	7.0	233K

study, has to be attributed to the fact that the transformation is suppressed until the relation of Eq. (6) is fulfilled. Values close to 2 for the exponent n, have been used in TRIP-assisted steels and represent a random orientation of shear band intersections [55,56]. Furthermore, Table 6 shows the obtained value of $\frac{\gamma_N}{N}$ from Eq. (6), i.e. the fault energy over the number of {111} faulted planes within the SF for the corresponding temperatures and loading states. The comparison between the measured and simulated volume fractions of martensite demonstrates that the proposed kinetic model is capable of fitting the martensite volume fraction evolution for different stress states.

Third, the martensite phase hardening law parameters are obtained by fitting the stress-strain curves that exhibit hardening due to phase transformation: simple tension at 293 K for AS-2 (Fig. 4b), simple tension at 77 K for AS-3 (Fig. 4c), simple tension at 233 K for AS-4 (Fig. 4d) and plane strain tension at 233 K for AS-4 (Fig. 4e). Since cruciform-shaped samples are used for the equibiaxial tension measurements, it is not possible to analytically compute the cruciform gauge stresses (due to the fact that cruciform samples do not have a defined gauge section, see Refs. [37,57]). Hence, only force and strain along the two loading directions are obtained from the cruciform experiments. Since gauge stress information is not available for the equibiaxial test on AS-1, the hardening law parameters of the martensite phase were set equal to the parameters for AS-2 because these two steels have similar compositions. The fitted hardening law parameters for martensite in all materials are shown in Table 5. Similarly, the values for L^{ss}, $L^{ss'}$, g^{ss}, $g^{ss'}$, q, D were set based on the literature, while τ_0, k_1, and g were varied to fit the response of the martensite phase. A single set of hardening parameters for the martensite phase was used for all simulated materials.

By fitting the martensite volume fraction evolution with strain on AS-1 and using the hardening law parameters for austenite and martensite (see above) it is possible to predict the stress in the test section of the cruciform sample. Fig. 6a shows the predicted equivalent stress-equivalent nonelastic strain evolution for the equibiaxial tension test. Similarly, the fitted kinetic model and hardening law parameters for AS-3 allow the prediction of the mechanical response under simple compression and torsion, shown in Fig. 6b, for which no experimental data is available.

The EPSC model is capable of predicting the crystallographic texture evolution, as mentioned earlier. The measured and simulated initial textures for AS-2 are shown in Fig. 7a. The predicted and measured deformation texture for AS-2 are compared in Fig. 7b. The comparison is performed for simple tension at 293 K, after 0.4 true strain. It is observed that the main trends in the texture evolution of the austenite phase are correctly predicted by the model, i.e. increase of the <111> fiber intensity and formation of a distinct "ring" pattern in the {002} and {022} pole figures. The predicted martensite texture exhibits similar features as the measured one. The starting crystallographic orientation of martensite grains, once they nucleate, is selected based on the identified T/2 and T/3 slip planes. The starting crystallographic orientation will primarily evolve due to plastic deformation. Therefore, both the martensite variant selection procedure and crystal reorientation, contribute to the match between predicted and measured textures.

6. Discussion

6.1. The effect of stress state on strain-induced α'-martensite transformation

Previous phenomenological kinetic models account for the role of the stress state as a function of macroscopic stress parameters through the Lode angle and stress triaxiality [11,12,14,58]. These models could not capture the influence of texture on the transformation, however they are able to capture the dependence of the martensite volume fraction for different macroscopic stress state. This implies that there must be some correlation between the macroscopic stress parameters and the parameters of the kinetic model presented in equations (3) and (4).

To investigate the relationship of x_α with the stress state, simulations are performed using the input for AS-3 material (Table 4) at 293K. The phase transformation is suppressed during the simulations and the texture evolution is turned off. Fig. 8 shows the predicted dependence of x_α with different stress states as function of the equivalent nonelastic strain. The x_α parameter exhibits a similar trend with stress state as the Lode angle since $\theta = -1$ for equibiaxial tension or SC, $\theta = 0$ for pure torsion and $\theta = 1$ for simple tension. As seen from Fig. 8, the proposed kinetic model predicts that simple tension (with higher x_α) leads to the formation of the largest amount of shear bands and potential martensite nucleation sites, followed by plane strain tension, torsion, simple compression and equibiaxial tension.

The proposed kinetic model predicts that the probability of martensite embryo nucleation at shear band intersections, which is controlled by the parameter β (Eq. (5)), decreases with changing the stress state in following order: equibiaxial tension, plane strain tension, simple tension, torsion and simple compression.

6.2. The effect of texture on the formation of potential nucleation sites

The extended Olson and Cohen kinetic model presented here relates the martensite fraction with the shear strain on the slip

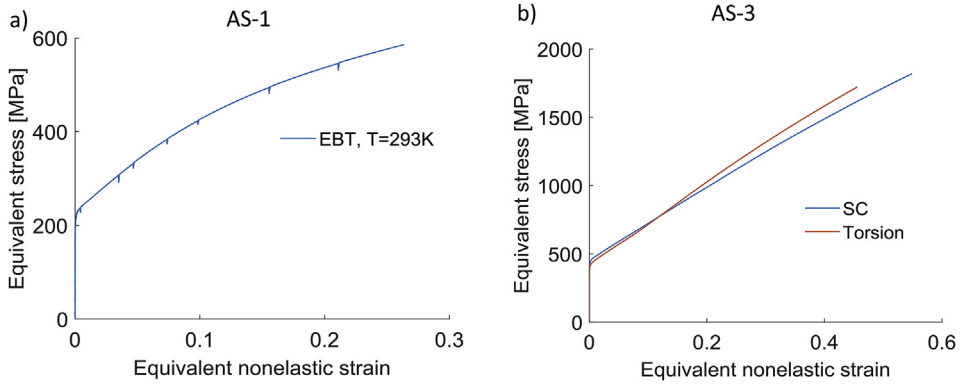

Fig. 6. Predictions of mechanical response for (a) EBT at room temperature (293 K) for AS-1 and (b) SC and torsion at 77 K for AS-3.

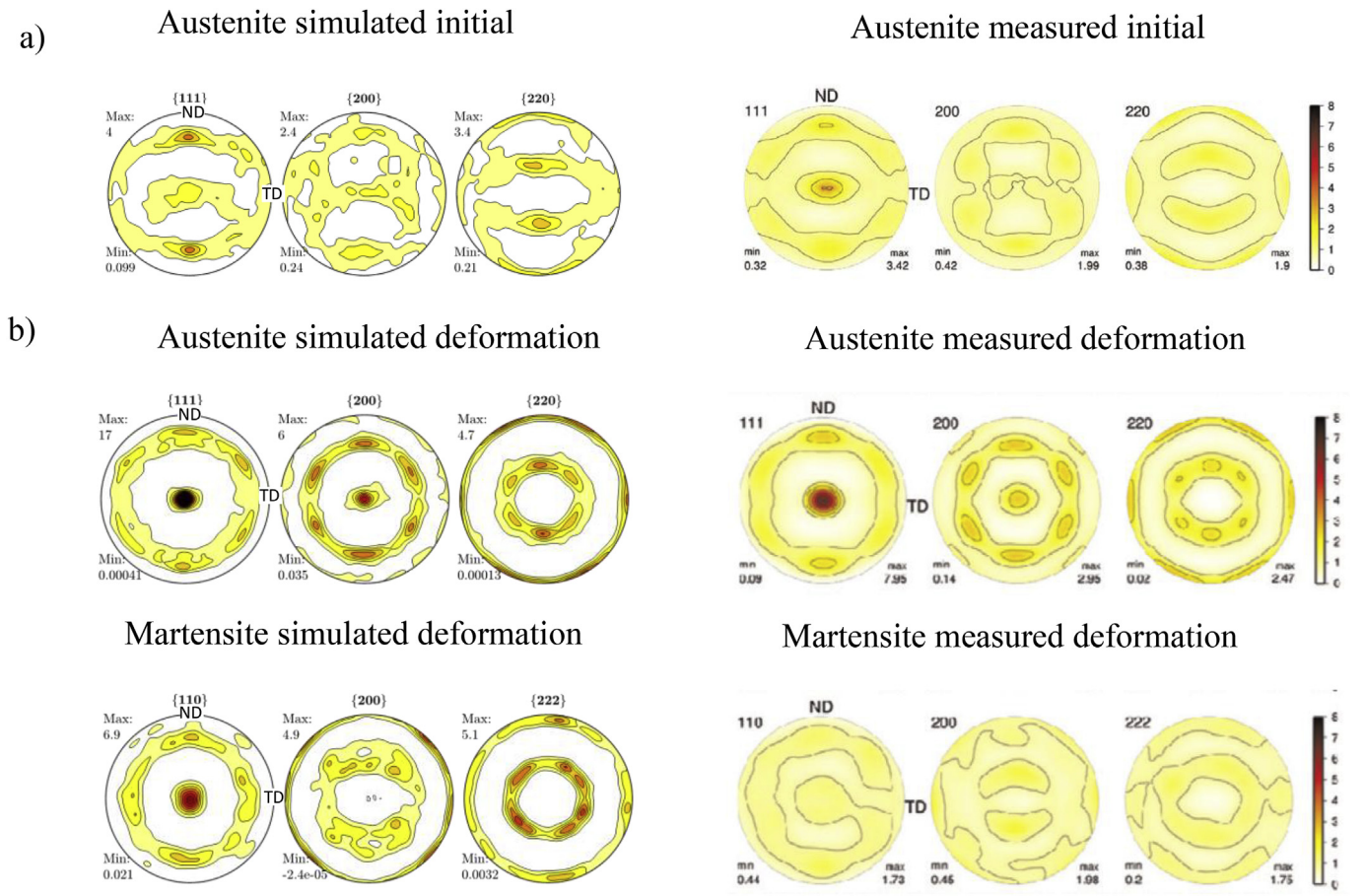

Fig. 7. (a) Pole figures showing the initial texture for AS-2 (simulated and measured). (b) Comparison of the measured and simulated textures after simple tension at room temperature to a true strain of 0.4 for austenite and martensite.

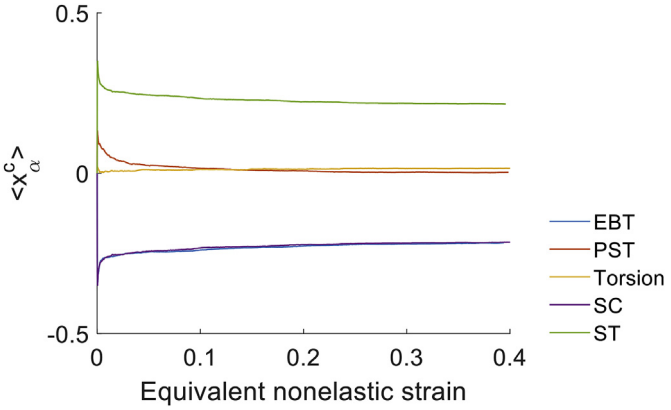

Fig. 8. The evolution of the volume average of the x_α parameter with strain for different stress states.

systems in each grain, while the rate of evolution of the martensite fraction is controlled by the parameter x_α and the stress triaxiality. The parameter x_α depends on the crystal orientation with respect to the loading direction and the stress state in the crystal, while the stress triaxiality (x_β) depends only on the stress state. Therefore, the effect of crystal orientation on the phase transformation is intrinsically accounted for by the parameter x_α. In contrast, the Lode angle parameter, although related to x_α, is dependent only on the macroscopic stress state and does not account for the effect of crystal orientation on the strain-induced phase transformation.

To study the effect of crystal orientation on the creation of potential nucleation sites, the stress state is fixed to simple tension or equibiaxial tension while the crystal orientation with respect to the tension axis is varied. The tension is enforced by imposing strain increments in the tension direction, while keeping the lateral normal stresses and all shear stresses at 0. The crystal orientation does not evolve during the simulations. The model input for AS-3 material at 293 K in Table 4 is used and martensite formation is suppressed. The parameter x_α is defined with Eq. (7), where the sum is over all the active slip systems. The predicted dependence of x_α on the direction of tension with respect to the crystal directions is shown in Fig. 9a, where contours of x_α are plotted on the inverse pole figures (IPF). The parameter x_α is calculated by applying simple tension to 0.02 true strain to single crystals in the direction determined with the IPF. The case when $x_\alpha > 0$ suggests more slip systems have preference to form wide SFWs, and vice versa for the case when $x_\alpha < 0$. Fig. 9a shows that x_α has minimum value for the case when ⟨001⟩ is parallel to the tension direction, while the maximum value is observed when ⟨011⟩ and ⟨111⟩ are parallel to the tension direction. Since the parameter α, is linearly proportional to x_α, the contours of x_α correspond to contours of α. According to the classical model of Olson and Cohen, the α parameter controls the evolution of volume fraction of shear bands (in the form of ε-martensite, twinning, SFs etc.). Therefore, more shear bands and more potential nucleation sites are predicted for ⟨011⟩ and ⟨111⟩ parallel to tension direction than for ⟨001⟩ parallel to tension direction. The prediction is consistent with the observations from

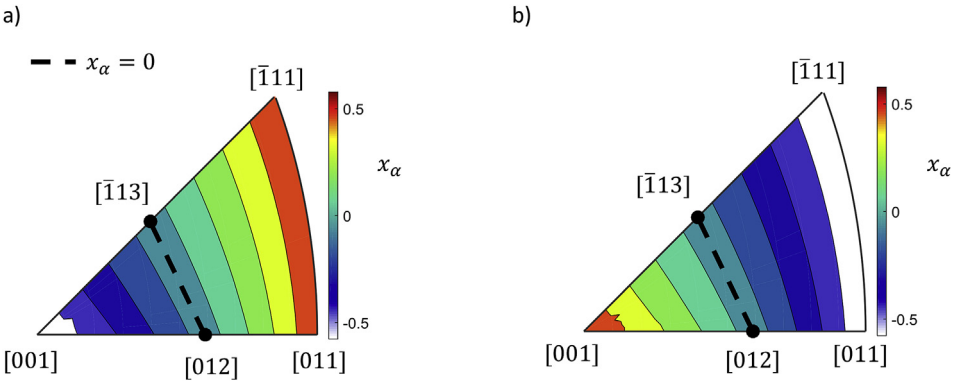

Fig. 9. Contours of x_α plotted on an IPF for (a) the tension direction and (b) the out-of-plane direction for in-plane equibiaxial tension.

Refs. [59–62]. Furthermore, the dependence of x_α on the SFW is in agreement with the Schmid factor analysis for partial dislocations presented in Ref. [4] where it is seen that under uniaxial loading, <111> and <011> orientations cause increase of the SFW and the formation of shear bands whereas <001> does not. It should be noted that the model is unable to distinguish whether these planar defects can be in the form of either ε-martensite, SFs (which are precursors of α-martensite) [4] or mechanical twins [24,25] (which can accommodate strain and even suppress the martensite formation) [63]. Such a consideration and distinction is beyond the scope of the present study.

From Eq. (7) it is seen that x_α depends only on the shear stresses resolved on the slip plane, and therefore x_α^c depends only on the deviatoric part of the stress tensor. Since the compressive deviatoric stress tensor is equal to the negative tensile deviatoric stress tensor, it follows that: $(x_\alpha)_{SC} = -(x_\alpha)_{ST}$. Furthermore, the deviatoric stress for the simple compression along one direction has the same ratio between its components as the deviatoric stress for the equibiaxial tension along the other two directions. This implies that $(x_\alpha)_{SC} = (x_\alpha)_{EBT} = -(x_\alpha)_{ST}$. To verify this, equibiaxial tension is applied to a set of crystal orientations with the same set up that was used to generate Fig. 9a. The equibiaxial tension boundary conditions are applied by imposing equal increments in normal stresses along directions 2 and 3, while the normal stress in the direction 1 and all shear stresses are maintained at 0. The parameter x_α is evaluated at 0.02 equivalent plastic strain. The model predicts that crystals with the <001> orientation parallel to the out-of-plane direction during in-plane equibiaxial tension possess the ideal conditions for shear band formation. The prediction is consistent with experimental observation reported in Ref. [4]. Since x_α is the same for simple compression and the equibiaxial tension, Fig. 9b is showing its dependence on the orientation of the compression direction with respect to the crystal directions. The model predicts that crystals with <001> parallel to the compression direction are favorably oriented for transformation, while the crystals compressed along <011> or <111> suppress the formation of shear bands. These prediction are in good agreement with the observations of Ref. [61].

6.3. The effect of α′-martensite on the mechanical response of austenitic steel

The model is used to simulate the mechanical response of austenitic steels while accounting for the contribution of the strain-induce α'-martensite to the strain hardening. The comparison between the measured and the simulated mechanical response shows that the model is capable of capturing the overall trends with the introduction of α'-martensite phase. However, several features of the response are not captured by the current model. For instance, the change in hardening rate after the yield point as seen in Fig. 4c and d, is not modeled accurately. The mechanical response before α'-martensite transformation is most likely governed by shear bands containing SFs, ε-martensite or twins, interacting with dislocations [16]. The effect of those shear bands on the mechanical response is not included in the current model.

The experimental stress-strain response of AS-4 steel during simple tension at 233 K (Fig. 4d) shows a drop of the hardening rate after the onset of the transformation. It has been observed with electron microscopy that, at low temperatures, the shear band intersections with α'-martensite do not hinder the motion of dislocations but they rather act as a "window" to let dislocations to pass through [64]. The model is however not able to capture such details in microstructural phenomena that cause softening. In addition, the transformation strain related to the formation of α'-martensite affects the intragranular stress fields both in the formed martensite and the parent austenite grain. The transformation strain in the model is assumed to be uniform over both the parent austenite and product martensite grain, while the stress of transforming martensite volume is assumed to be equal to the stress of the already nucleated martensite grain. The simplifying assumptions are likely contributing to the mismatch between the measured and the simulated stress-strain curves during the α'-martensite formation shown in Fig. 4d.

7. Conclusion

A crystallography-based extension to the classical Olson-Cohen kinetic model is presented. The extended phase transformation kinetic model sensitive to the magnitude of stress, stress state and crystal orientation is coupled with the EPSC crystal plasticity model. The combined model is applied to study the role of stress state and crystallographic orientation on the strain-induced austenite to α'-martensite transformation while simulating the mechanical response of metastable austenitic steels. The main conclusions are:

1. The proposed modifications account for the physics-based effect of the stress state on the strain-induced α'-marteniste transformation in the following manner: (i) The resolved shear stress in the direction perpendicular to the Burgers vector changes the SFW of the dislocations. The SFW controls the formation of shear bands, i.e. ε-martensite, twins and SFs, and affects the number of potential nucleation sites for α'-martensite. (ii) The stress triaxiality affects the probability of α'-martensite formation at an existing nucleation site, as proposed in older modifications of the model.
2. Consistent with previous experimental observations, the model predicts that more nucleation sites for α'-martensite are

generated for crystal orientations which have ⟨011⟩ and ⟨111⟩ parallel to the uniaxial tension. The trend is reversed for simple compression. In analogue, the crystal orientation with the <001> parallel to the out-of-plane direction during in-plane equibiaxial tension, is the most favorable orientation for the formation of nucleation sites for α'-martensite.

3. The introduction of α'-martensite in the model captures the overall work hardening response. Mismatches between the modeled and experimental mechanical response are due to simplifying model assumptions related to the state of transforming martensite volume and the effect of shear bands (i.e. either SFs, ε-martensite or mechanical twins), which will be considered in future works.

Acknowledgements

M.Z. and M.K. are grateful for the financial support to the U.S. National Science Foundation under the CAREER grant no. CMMI-1650641. M.Z., M.V.U., and H.V.S. acknowledge the financial support of the European Research Council through the ERC advanced grant MULTIAX (339245). M.Z. also acknowledges the financial support from the University of New Hampshire's Dissertation Year Fellowship program.

Appendix A. SFW

The dissociation of a perfect dislocation into Shockley partials on all the $\{111\}\bar{1}10$ slip systems is considered. The configuration in Fig. A1a shows one out of the 12 slip systems within a crystal, containing 2 partial dislocations. Definitions of the unit Burgers vector direction of the perfect dislocation, $\hat{\mathbf{b}}$, the unit slip plane normal, $\hat{\mathbf{n}}$, and the unit dislocation line direction, $\hat{\mathbf{l}}$, are consistent with the conventions from Ref. [65]. In the derivation presented here, we do not use the terms leading and trailing partial since their definition requires knowledge of the sense of the dislocation velocity and changes with the change of the sense of velocity. Instead, we define the left and right partial dislocations and derive the expression for the SFW which is independent of the sense of the dislocation velocity. We can determine the left and right partial for each slip system using the Thompson tetrahedron and axiom 10-1 from Ref. [65]:

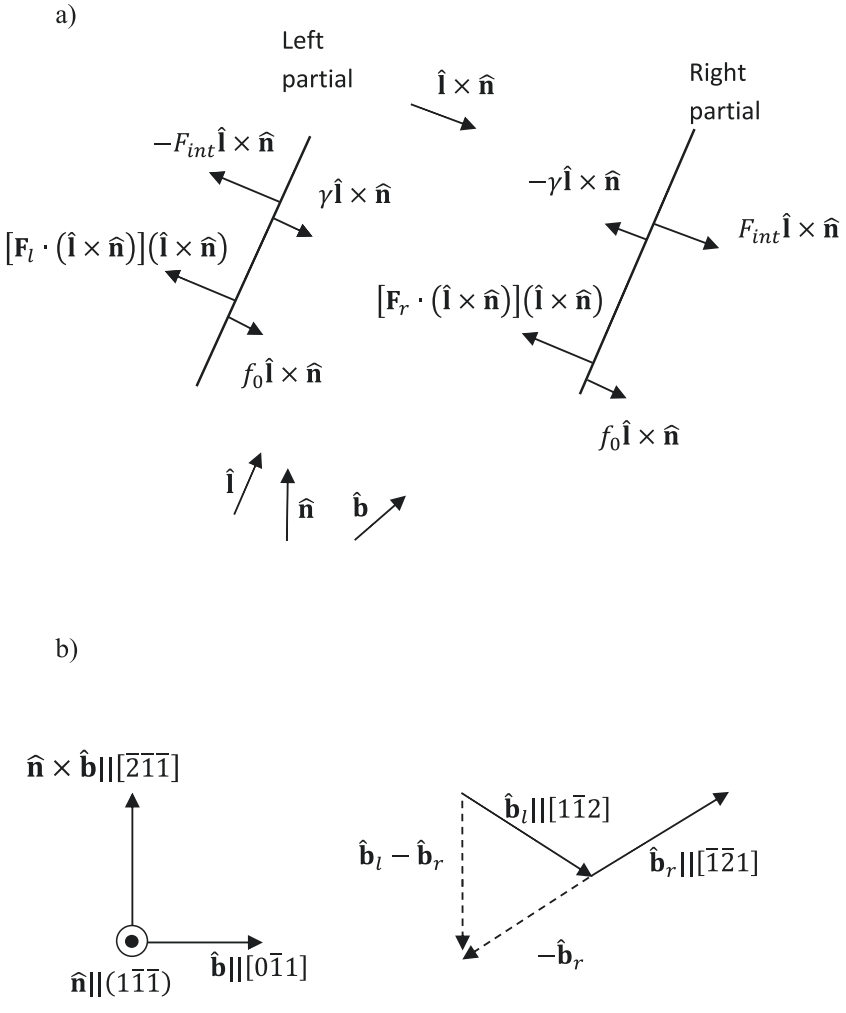

Fig. A1. (a) Force balance on two partial dislocations with dislocation line direction, $\hat{\mathbf{l}}$, moving to the left on a slip system determined with burgers direction, $\hat{\mathbf{b}}$, and normal direction, $\hat{\mathbf{n}}$. (b) Burgers vectors of the left partial, $\hat{\mathbf{b}}_l$, and right partial, $\hat{\mathbf{b}}_r$, on a slip system $[0\bar{1}1](1\bar{1}1)$ and direction, $\hat{\mathbf{b}}_l - \hat{\mathbf{b}}_r$, in the slip plane related to increase of the SFW.

"Viewing the perfect dislocation from outside the tetrahedron and along the positive sense of the line, the intrinsic stacking-fault arrangement is achieved by placing the Greek-Roman partial on the viewer's left and the Roman-Greek partial on the right; viewed in the positive sense from inside the tetrahedron, the intrinsic arrangement is achieved by placing the Roman-Greek partial on the left and Greek-Roman partial on the right."

plane normal / perfect		left partial (1)		right partial (2)
(1 -1 -1)	[0 -1 1] =	[1 -1 2]	+	[-1 -2 1]
(1 -1 -1)	[1 0 1] =	[1 -1 2]	+	[2 1 1]
(1 -1 -1)	[1 1 0] =	[1 2 -1]	+	[2 1 1]
(1 1 1)	[0 -1 1] =	[1 -2 1]	+	[-1 -1 2]
(1 1 1)	[-1 0 1] =	[-2 1 1]	+	[-1 -1 2]
(1 1 1)	[-1 1 0] =	[-2 1 1]	+	[-1 2 -1]
(-1 -1 1)	[0 1 1] =	[-1 2 1]	+	[1 1 2]
(-1 -1 1)	[1 0 1] =	[2 -1 1]	+	[1 1 2]
(-1 -1 1)	[-1 1 0] =	[-1 2 1]	+	[-2 1 -1]
(-1 1 -1)	[0 1 1] =	[-1 1 2]	+	[1 2 1]
(-1 1 -1)	[-1 0 1] =	[-1 1 2]	+	[-2 -1 1]
(-1 1 -1)	[1 1 0] =	[2 1 -1]	+	[1 2 1]

To find the SFW, the force equilibrium of the partial dislocations in the direction of motion is considered [26,65]. Fig A1a shows the case when dislocations move to the left under the action of applied stress. However, the sense of the direction of motion is not assumed in the derivation of the separation between the partial dislocations. Therefore, the derived expressions work for both cases when the left partial is leading and when the left partial is trailing. The force balance in the direction of motion is:

$$\left[\mathrm{F}_l\cdot\left(\hat{\mathrm{l}}\times\hat{\mathrm{n}}\right)\right]\left(\hat{\mathrm{l}}\times\hat{\mathrm{n}}\right)+\gamma\left(\hat{\mathrm{l}}\times\hat{\mathrm{n}}\right)-F_{int}\left(\hat{\mathrm{l}}\times\hat{\mathrm{n}}\right)-f_0\hat{\mathrm{v}}=0 \quad (A1)$$

$$\left[\mathrm{F}_r\cdot\left(\hat{\mathrm{l}}\times\hat{\mathrm{n}}\right)\right]\left(\hat{\mathrm{l}}\times\hat{\mathrm{n}}\right)-\gamma\left(\hat{\mathrm{l}}\times\hat{\mathrm{n}}\right)+F_{int}\left(\hat{\mathrm{l}}\times\hat{\mathrm{n}}\right)-f_0\hat{\mathrm{v}}=0 \quad (A2)$$

where F_l, F_r are the forces on the left and right partial due to applied stress, γ is the force equal to intrinsic SFE, trying to constrict the partials, F_{int} is the interaction force between the partials, repulsing them, f_0 is a friction force acting in the direction opposite to the velocity of the dislocations and $\hat{\mathrm{v}}$ is the normalized velocity of the dislocations. The forces on the left and the right partial due to the applied stress are [65]:

$$\mathrm{F}_l=(\mathrm{b}_l\,\sigma^c)\times\hat{\mathrm{l}} \quad (A3)$$

$$\mathrm{F}_r=(\mathrm{b}_r\,\sigma^c)\times\hat{\mathrm{l}} \quad (A4)$$

where b_l and b_r are the Burgers vectors of the left and right partial, respectively. Projecting the forces on the dislocations in the direction of motion gives:

$$\mathrm{F}_l\cdot\left(\hat{\mathrm{l}}\times\hat{\mathrm{n}}\right)=-(\mathrm{b}_l\,\sigma^c)\cdot\hat{\mathrm{n}}=-b_p\tau_l \quad (A5)$$

$$\mathrm{F}_r\cdot\left(\hat{\mathrm{l}}\times\hat{\mathrm{n}}\right)=-(\mathrm{b}_r\,\sigma^c)\cdot\hat{\mathrm{n}}=-b_p\tau_r \quad (A6)$$

where τ_l and τ_r are the resolved shear stresses on the left and right partial, respectively, and b_p is the magnitude of the Burgers vector of the partial dislocations. The interaction force between the partials is [65]:

$$F_{int}=\frac{c(\theta,\mu,\nu,b_p)}{2d} \quad (A7)$$

with:

$$c(\theta,\mu,\nu,b_p)=\frac{\mu b_p^2}{\pi}\left[\left(\hat{\mathrm{b}}_l\cdot\hat{\mathrm{l}}\right)\left(\hat{\mathrm{b}}_r\cdot\hat{\mathrm{l}}\right)+\frac{1}{1-\nu}\left(\hat{\mathrm{b}}_l\times\hat{\mathrm{l}}\right)\cdot\left(\hat{\mathrm{b}}_r\times\hat{\mathrm{l}}\right)\right] \quad (A8)$$

and d is the SFW. Subtracting (A2) from (A1) and using (A5), (A6), and (A7) allows expressing the SFW as:

$$d=\frac{c(\theta,\mu,\nu,b_p)}{2\gamma+(\mathrm{b}_r\sigma^c)\cdot\hat{\mathrm{n}}-(\mathrm{b}_l\sigma^c)\cdot\hat{\mathrm{n}}}. \quad (A9)$$

From Eq. (A9), it follows that the SFW is proportional to the shear stress resolved on the slip plane in the direction perpendicular to the burgers vector of the perfect dislocation:

$$d=c\,/\left[2\gamma-b_p\left(\left(\hat{\mathrm{b}}_l-\hat{\mathrm{b}}_r\right)\sigma^c\right)\cdot\hat{\mathrm{n}}\right]. \quad (A10)$$

Fig. A1b shows the situation for the $(1\bar{1}1)[0\bar{1}1]$ slip system. From Fig. A1b, it can be seen that the shear stress in the direction $\hat{\mathrm{b}}_l-\hat{\mathrm{b}}_r$ causes positive resolved shear stress on the left partial and negative resolved shear stress on the right partial. Therefore, the left partial will move to the left under the action of stress, while the right partial will move to the right i.e. the SFW will increase. The presence of shear stress in the direction $-(\hat{\mathrm{b}}_l-\hat{\mathrm{b}}_r)$ will have the opposite effect i.e. the SFW will decrease [66].

In the derivation of Eq. (A10), the SF is assumed to include one (111) plane, i.e. an intrinsic SF. It has been experimentally observed that occurrence of one wide SF triggers dissociation on neighboring (111) planes, leading to thickening of the fault [46]. Such thick fault can be treated as a SF bounded with partial superdislocations [19]. If the thick fault includes N intrinsic SFs on N (111) planes, the partial superdislocation burgers vector is Nb_p. Therefore, the SFW of the thick fault is:

$$d=cN^2\,/\left[2\gamma_N-Nb_p\left(\left(\hat{\mathrm{b}}_l-\hat{\mathrm{b}}_r\right)\sigma^c\right)\cdot\hat{\mathrm{n}}\right] \quad (A11)$$

where γ_N is the fault energy. The fault energy is related to intrinsic SFE and the surface energy of the fault and can either be constant in the case of a mechanical twin, or decrease with increasing N in the case of ε-martensite formation [3,19].

Appendix B. Crystal lattice reorientation during the strain-induced martensitic transformation and the associated phase transformation strain

To consistently derive the crystal orientation of the martensite grains and the associated phase transformation strain, we follow the mechanisms of strain-induced transformations as described in Refs. [1,67,68]. In the strain-induced transformation, martensite forms at the intersection of two shear bands. The atoms in one

shear band have positions corresponding to T/2 shear, where T refers to twinning shear. The twinning shear is $T = \frac{b_p}{d_{111}}$, where d_{111} is the spacing between the $\{111\}_\gamma$ planes. The T/2 shear structure can be formed from ε-martensite by shuffles on every 2nd $\{0001\}_\varepsilon$ plane for $\frac{a_\gamma}{12}1\bar{1}2_\gamma$. The shuffle transforms the $\{1\bar{1}01\}_\varepsilon$ planes into uniformly distorted $\{111\}_\gamma$ planes. Next, the partial dislocations in austenite, averaging one on every three $\{111\}_\gamma$ planes, pass through the uniformly distorted $\{111\}_\gamma$ planes in the T/2 structure. These partial dislocations are part of the other shear band causing the T/3 shear in the T/2 shear band. The intersection of the T/2 and T/3 shear bands has a bcc structure. Additionally, there is a volume increase of 2.59%, determined by the lattice parameters of austenite, $a_\gamma = 0.3589$ nm, and martensite, $a_{\alpha'} = 0.2873$ nm [28]. The orientation relationship between austenite, ε-martensite and α'-martensite has been reported to be [67]:

$$\{111\}_\gamma \parallel \{0001\}_\varepsilon \parallel \{110\}_{\alpha'} \tag{B1}$$

$$110_\gamma \parallel 2\bar{1}\bar{1}0_\varepsilon \parallel 111_{\alpha'}. \tag{B2}$$

In the model, we first identify the two slip systems that will form T/2 and T/3 shear bands. We assume that the slip system with the highest SFW will create the T/2 shear band. In fact, we assume that this slip system will form ε-martensite, which is converted to T/2 structure by shuffles during the passage of the partial dislocations from the T/3 shear band. Depending on the direction of the shuffle in the ε-martensite, the product structure will be identical to the structure created by uniform shearing of austenite for T/2 in the shearing direction and sense of one of the possible leading partials on T/2 plane. In general, the shearing direction and sense of the leading partial is in $\hat{b}_l$, if the resolved shear stress (RSS) on $0\bar{1}1\{111\}_\gamma$ slip systems listed in appendix B is greater than zero, and in $-\hat{b}_r$ if RSS is lower than zero. Using these rules and checking all possibilities, we can determine all possible leading partial directions and senses on T/2 plane. Next, we choose the plane with the highest RSS on the leading partial to be the T/3 plane, with certain constraints originating from the relationship between T/2 and T/3 shears shown in Ref. [68]. In their paper, Bogers and Burgers show that there is a specific relationship between T/2 and T/3 shear planes and directions to produce the bcc structure. By examining a tetrahedron made from four {111} planes, they concluded that if T/3 shear is applied in leading partial shearing direction, only two {111} planes change their shape and only one 110 direction gets longer. The T/2 shear needs to be on one of the deformed {111} planes and perpendicular to the longer 110 direction. If there are no active planes which satisfy these relationships with T/2 plane, the search is expanded to include all slip planes in a crystal. Once we have determined the T/3 and T/2 planes and the directions, we can define the martensite orientation, which satisfies (B1) and (B2) relations.

The deformation gradient related to the austenite to α'-martensite transformation can be written as:

$$\mathbf{F}^{pt} = \mathbf{F}^{vol}\mathbf{F}^{T/3}\mathbf{F}^{T/2}, \tag{B3}$$

where $\mathbf{F}^{T/2}$ is the deformation gradient describing the shearing on the T/2 plane, $\mathbf{F}^{T/3}$ is the deformation gradient describing the shearing on the T/3 plane and $\mathbf{F}^{vol}$ is the deformation gradient describing the volume change, defined as the volumetric part of the Bain deformation gradient. The Olson-Cohen model assumes that shear bands constitute a fraction of plastic deformation. The volume fraction of shear bands is calculated from plastic strain with Eqs. (9b) and (10b). Therefore, at any instant in simulation plastic strain contains $\mathbf{F}^{T/2}$ and $\mathbf{F}^{T/3}$ deformation. Since the shear part of the phase transformation is already accounted for by the plastic strain, the phase transformation strain is simply calculated as:

$$\boldsymbol{\varepsilon}^{pt} = \frac{\left(\mathbf{F}^{vol}\right)^T\mathbf{F}^{vol} - \mathbf{I}}{2}. \tag{B4}$$

Appendix C. Supplementary data

Supplementary data to this article can be found online at https://doi.org/10.1016/j.actamat.2018.12.060.

References

[1] G.B. Olson, M. Cohen, A mechanism for the strain-induced nucleation of martensitic transformations, J. Less Common Met. 28 (1972) 107–118.
[2] G.B. Olson, M. Cohen, Kinetics of strain-induced martensitic nucleation, Metallurgical Transactions A 6 (1975) 791.
[3] J. Talonen, H. Hänninen, Formation of shear bands and strain-induced martensite during plastic deformation of metastable austenitic stainless steels, Acta Mater. 55 (2007) 6108–6118.
[4] E. Polatidis, W.N. Hsu, M. Šmíd, T. Panzner, S. Chakrabarty, P. Pant, H. Van Swygenhoven, Suppressed martensitic transformation under biaxial loading in low stacking fault energy metastable austenitic steels, Scripta Mater. 147 (2018) 27–32.
[5] Y.B. Das, A.N. Forsey, T.H. Simm, K.M. Perkins, M.E. Fitzpatrick, S. Gungor, R.J. Moat, In situ observation of strain and phase transformation in plastically deformed 301 austenitic stainless steel, Mater. Des. 112 (2016) 107–116.
[6] G.B. Olson, Effects of stress and deformation on martensitic formation, in: H. Aaronson (Ed.), Encyclopedia of Materials, Elsevier, 2002.
[7] G.B. Olson, M. Azrin, Transformation behavior of TRIP steels, Metallurgical Transactions A 9 (1978) 713–721.
[8] G.N. Haidemenopoulos, N. Aravas, I. Bellas, Kinetics of strain-induced transformation of dispersed austenite in low-alloy TRIP steels, Mater. Sci. Eng., A 615 (2014) 416–423.
[9] K. Yukio, Kinetics of Deformation-Induced Transformation of Dispersed Austenite in Two Alloy Systems, Master of Science: Massachusetts Institute of Technology, 1987.
[10] S.S. Hecker, M.G. Stout, K.P. Staudhammer, J.L. Smith, Effects of strain state and strain rate on deformation-induced transformation in 304 stainless steel: Part I. Magnetic measurements and mechanical behavior, Metallurgical Transactions A 13 (1982) 619–626.
[11] A.A. Lebedev, V.V. Kosarchuk, Influence of phase transformations on the mechanical properties of austenitic stainless steels, Int. J. Plast. 16 (2000) 749–767.
[12] A.M. Beese, D. Mohr, Effect of stress triaxiality and Lode angle on the kinetics of strain-induced austenite-to-martensite transformation, Acta Mater. 59 (2011) 2589–2600.
[13] V. Talyan, R.H. Wagoner, J.K. Lee, Formability of stainless steel, Metall. Mater. Trans. 29 (1998) 2161–2172.
[14] H. Kim, J. Lee, F. Barlat, D. Kim, M.-G. Lee, Experiment and modeling to investigate the effect of stress state, strain and temperature on martensitic phase transformation in TRIP-assisted steel, Acta Mater. 97 (2015) 435–444.
[15] H.N. Han, C.G. Lee, C.-S. Oh, T.-H. Lee, S.-J. Kim, A model for deformation behavior and mechanically induced martensitic transformation of metastable austenitic steel, Acta Mater. 52 (2004) 5203–5214.
[16] Y.F. Shen, X.X. Li, X. Sun, Y.D. Wang, L. Zuo, Twinning and martensite in a 304 austenitic stainless steel, Mater. Sci. Eng., A 552 (2012) 514–522.
[17] M.P. Miller, D.L. McDowell, The effect of stress-state on the large strain inelastic deformation behavior of 304L stainless steel, J. Eng. Mater. Technol. 118 (1996) 28–36.
[18] T. Iwamoto, T. Tsuta, Y. Tomita, Investigation on deformation mode dependence of strain-induced martensitic transformation in trip steels and modelling of transformation kinetics, Int. J. Mech. Sci. 40 (1998) 173–182.
[19] G.B. Olson, M. Cohen, A general mechanism of martensitic nucleation: Part I. General concepts and the FCC → HCP transformation, Metallurgical Transactions A 7 (1976) 1897–1904.
[20] R.G. Stringfellow, D.M. Parks, G.B. Olson, A constitutive model for transformation plasticity accompanying strain-induced martensitic transformations in metastable austenitic steels, Acta Metall. Mater. 40 (1992) 1703–1716.
[21] P. Santacreu, J.C. Glez, G. Chinouilh, T. Froehlich, Behaviour Model of Austenitic Stainless Steels for Automotive Structural Parts, 2006.
[22] M. Mansourinejad, M. Ketabchi, Modification of Olson–Cohen model for predicting stress-state dependency of martensitic transformation, Mater. Sci. Technol. 33 (2017) 1948–1954.
[23] S.M. Copley, B.H. Kear, The dependence of the width of a dissociated dislocation on dislocation velocity, Acta Metall. 16 (1968) 227–231.
[24] S. Martin, C. Ullrich, D. Rafaja, Deformation of austenitic CrMnNi TRIP/TWIP steels: nature and role of the ε–martensite, Mater. Today: Proceedings 2

(2015) S643–S646.
[25] C. Ullrich, R. Eckner, L. Krüger, S. Martin, V. Klemm, D. Rafaja, Interplay of microstructure defects in austenitic steel with medium stacking fault energy, Mater. Sci. Eng., A 649 (2016) 390–399.
[26] T.S. Byun, On the stress dependence of partial dislocation separation and deformation microstructure in austenitic stainless steels, Acta Mater. 51 (2003) 3063–3071.
[27] R.J. McCabe, I.J. Beyerlein, J.S. Carpenter, N.A. Mara, The critical role of grain orientation and applied stress in nanoscale twinning, Nat. Commun. 5 (2014) 3806.
[28] H. Wang, Y. Jeong, B. Clausen, Y. Liu, R.J. McCabe, F. Barlat, C.N. Tomé, Effect of martensitic phase transformation on the behavior of 304 austenitic stainless steel under tension, Mater. Sci. Eng., A 649 (2016) 174–183.
[29] P.A. Turner, C.N. Tomé, A study of residual stresses in Zircaloy-2 with rod texture, Acta Metall. Mater. 42 (1994) 4143–4153.
[30] C.J. Neil, J.A. Wollmershauser, B. Clausen, C.N. Tomé, S.R. Agnew, Modeling lattice strain evolution at finite strains and experimental verification for copper and stainless steel using in situ neutron diffraction, Int. J. Plast. 26 (2010) 1772–1791.
[31] M. Zecevic, M. Knezevic, Latent hardening within the elasto-plastic self-consistent polycrystal homogenization to enable the prediction of anisotropy of AA6022-T4 sheets, Int. J. Plast. 105 (2018) 141–163.
[32] M. Zecevic, M. Knezevic, A dislocation density based elasto-plastic self-consistent model for the prediction of cyclic deformation: application to Al6022-T4, Int. J. Plast. 72 (2015) 200–217.
[33] M. Zecevic, M. Knezevic, I.J. Beyerlein, C.N. Tomé, An elasto-plastic self-consistent model with hardening based on dislocation density, twinning and de-twinning: application to strain path changes in HCP metals, Mater. Sci. Eng. A 638 (2015) 262–274.
[34] M. Zecevic, I.J. Beyerlein, M. Knezevic, Coupling elasto-plastic self-consistent crystal plasticity and implicit finite elements: applications to compression, cyclic tension-compression, and bending to large strains, Int. J. Plast. 93 (2017) 187–211.
[35] M. Zecevic, Y.P. Korkolis, T. Kuwabara, M. Knezevic, Dual-phase steel sheets under cyclic tension–compression to large strains: experiments and crystal plasticity modeling, J. Mech. Phys. Solid. 96 (2016) 65–87.
[36] M. Zecevic, M. Knezevic, Modeling of sheet metal forming based on implicit embedding of the elasto-plastic self-consistent formulation in shell elements: application to cup drawing of AA6022-T4, JOM (J. Occup. Med.) 69 (2017) 922–929.
[37] S. Van Petegem, J. Wagner, T. Panzner, M.V. Upadhyay, T.T.T. Trang, H. Van Swygenhoven, In-situ neutron diffraction during biaxial deformation, Acta Mater. 105 (2016) 404–416.
[38] U. Stuhr, M. Grosse, W. Wagner, The TOF-strain scanner POLDI with multiple frame overlap—concept and performance, Mater. Sci. Eng., A 437 (2006) 134–138.
[39] U. Stuhr, H. Spitzer, J. Egger, A. Hofer, P. Rasmussen, D. Graf, A. Bollhalder, M. Schild, G. Bauer, W. Wagner, Time-of-flight diffraction with multiple frame overlap Part II: the strain scanner POLDI at PSI, Nucl. Instrum. Methods Phys. Res. Sect. A Accel. Spectrom. Detect. Assoc. Equip. 545 (2005) 330–338.
[40] O. Arnold, J.C. Bilheux, J.M. Borreguero, A. Buts, S.I. Campbell, L. Chapon, M. Doucet, N. Draper, R. Ferraz Leal, M.A. Gigg, V.E. Lynch, A. Markvardsen, D.J. Mikkelson, R.L. Mikkelson, R. Miller, K. Palmen, P. Parker, G. Passos, T.G. Perring, P.F. Peterson, S. Ren, M.A. Reuter, A.T. Savici, J.W. Taylor, R.J. Taylor, R. Tolchenov, W. Zhou, J. Zikovsky, Mantid—data analysis and visualization package for neutron scattering and μ SR experiments, Nucl. Instrum. Methods Phys. Res. Sect. A Accel. Spectrom. Detect. Assoc. Equip. 764 (2014) 156–166.
[41] Y. Tomita, T. Iwamoto, Computational prediction of deformation behavior of TRIP steels under cyclic loading, Int. J. Mech. Sci. 43 (2001) 2017–2034.
[42] Y. Tomita, T. Iwamoto, Constitutive modeling of trip steel and its application to the improvement of mechanical properties, Int. J. Mech. Sci. 37 (1995) 1295–1305.
[43] T. Iwamoto, T. Tsuta, Computational simulation on deformation behavior of CT specimens of TRIP steel under mode I loading for evaluation of fracture toughness, Int. J. Plast. 18 (2002) 1583–1606.
[44] W.J. Dan, S.H. Li, W.G. Zhang, Z.Q. Lin, The effect of strain-induced martensitic transformation on mechanical properties of TRIP steel, Mater. Des. 29 (2008) 604–612.
[45] J. Talonen, H. Hänninen, P. Nenonen, G. Pape, Effect of strain rate on the strain-induced γ → α′-martensite transformation and mechanical properties of austenitic stainless steels, Metall. Mater. Trans. 36 (2005) 421–432.
[46] H. Fujita, S. Ueda, Stacking faults and f.c.c. (γ) → h.c.p. (ε) transformation in 188-type stainless steel, Acta Metall. 20 (1972) 759–767.
[47] E.J. Mittemeijer. Fundamentals of Materials Science, Springer-Verlag Berlin Heidelberg.
[48] J.R. Patel, M. Cohen, Criterion for the action of applied stress in the martensitic transformation, Acta Metall. 1 (1953) 531–538.
[49] I.J. Beyerlein, C.N. Tomé, A dislocation-based constitutive law for pure Zr including temperature effects, Int. J. Plast. 24 (2008) 867–895.
[50] R. Masson, M. Bornert, P. Suquet, A. Zaoui, An affine formulation for the prediction of the effective properties of nonlinear composites and polycrystals, J. Mech. Phys. Solid. 48 (2000) 1203–1227.
[51] R. Lebensohn, D. Solas, G. Canova, Y. Brechet, Modelling damage of Al-Zn-Mg alloys, Acta Mater. 44 (1996) 315–325.
[52] F. Bachmann, R. Hielscher, H. Schaeben, Texture analysis with MTEX–free and open source software toolbox, Solid State Phenom. 160 (2010) 63–68.
[53] D. DeMania, The Influence of Martensitic Transformation on the Formability of 304L Stainless Steel Sheet, MS thesis, MIT, Cambridge,MA, 1995.
[54] N. Meysam, M. Hamed, Processing of fine grained AISI 304L austenitic stainless steel by cold rolling and high-temperature short-term annealing, Mater. Res. Express 5 (2018), 056529.
[55] D. Krizan, B.C. De Cooman, Analysis of the strain-induced martensitic transformation of retained austenite in cold rolled micro-alloyed TRIP steel, Steel Res. Int. 79 (2008) 513–522.
[56] L. Samek, E. De Moor, J. Penning, B.C. De Cooman, Influence of alloying elements on the kinetics of strain-induced martensitic nucleation in low-alloy, multiphase high-strength steels, Metall. Mater. Trans. 37 (2006) 109–124.
[57] M.V. Upadhyay, S. Van Petegem, T. Panzner, R.A. Lebensohn, H. Van Swygenhoven, Study of lattice strain evolution during biaxial deformation of stainless steel using a finite element and fast Fourier transform based multi-scale approach, Acta Mater. 118 (2016) 28–43.
[58] M. Sitko, B. Skoczeń, Effect of γ–α′ phase transformation on plastic adaptation to cyclic loads at cryogenic temperatures, Int. J. Solid Struct. 49 (2012) 613–634.
[59] W.G. Burgers, J.A. Klostermann, Influence of the direction of deformation on the transition of austenite into martensite, Acta Metall. 13 (1965) 568–572.
[60] R. Lagnebor, Acta Metall. 12 (1964).
[61] D. Goodchild, W.T. Roberts, D.V. Wilson, Plastic deformation and phase transformation in textured austenitic stainless steel, Acta Metall. 18 (1970) 1137–1145.
[62] B. Petit, N. Gey, M. Cherkaoui, B. Bolle, M. Humbert, Deformation behavior and microstructure/texture evolution of an annealed 304 AISI stainless steel sheet. Experimental and micromechanical modeling, Int. J. Plast. 23 (2007) 323–341.
[63] M.M. Wang, C.C. Tasan, D. Ponge, A. Kostka, D. Raabe, Smaller is less stable: size effects on twinning vs. transformation of reverted austenite in TRIP-maraging steels, Acta Mater. 79 (2014) 268–281.
[64] T. Suzuki, H. Kojima, K. Suzuki, T. Hashimoto, M. Ichihara, An experimental study of the martensite nucleation and growth in 18/8 stainless steel, Acta Metall. 25 (1977) 1151–1162.
[65] J.P. Hirth, J. Lothe, Theory of Dislocations, New York, 1968.
[66] J.-B. Baudouin, G. Monnet, M. Perez, C. Domain, A. Nomoto, Effect of the applied stress and the friction stress on the dislocation dissociation in face centered cubic metals, Mater. Lett. 97 (2013) 93–96.
[67] L. Bracke, L. Kestens, J. Penning, Transformation mechanism of α′-martensite in an austenitic Fe–Mn–C–N alloy, Scripta Mater. 57 (2007) 385–388.
[68] A.J. Bogers, W.G. Burgers, Partial dislocations on the {110} planes in the B.C.C. lattice and the transition of the F.C.C. into the B.C.C. lattice, Acta Metall. 12 (1964) 255–261.